Time-resolved *in situ* synchrotron-microCT: 4D deformation of bone and bone analogues using digital volume correlation

Marta Peña Fernández [1,2,*], Alexander P. Kao [1], Roxane Bonithon [1], David Howells [3], Andrew J. Bodey [4], Kazimir Wanelik [4], Frank Witte [5,6], Richard Johnston [3], Hari Arora [3], Gianluca Tozzi [1]

1. Zeiss Global Centre, School of Mechanical and Design Engineering, University of Portsmouth, Portsmouth, UK.
2. School of Engineering and Physical Sciences, Heriot-Watt University, Edinburgh, UK.
3. Faculty of Science and Engineering, Swansea University, Swansea, UK.
4. Diamond Light Source, Oxfordshire, UK.
5. Biotrics Bioimplants AG, Berlin, Germany.
6. Department of Prosthodontics, Geriatric Dentistry and Craniomandibular Disorders, Charité - Universitätsmedizin Berlin, Berlin, Germany.

 *Corresponding author:
Marta Peña Fernández, PhD
Heriot-Watt University
School of Engineering and Physical Sciences (EPS)
Institute of Mechanical, Process and Energy Engineering (IMPEE)
James Nasmyth Building, Room JN 2.24
Edinburgh, EH14 4AS, UK
Email: M.Pena_Fernandez@hw.ac.uk

Abstract

Digital volume correlation (DVC) in combination with high-resolution micro-computed tomography (microCT) imaging and *in situ* mechanical testing is gaining popularity for quantifying 3D full-field strains in bone and biomaterials. However, traditional *in situ* time-lapsed (i.e., interrupted) mechanical testing cannot fully capture the dynamic strain mechanisms in viscoelastic biological materials. The aim of this study was to investigate the time-resolved deformation of bone structures and analogues via continuous *in situ* synchrotron-radiation microCT (SR-microCT) compression and DVC to gain a better insight into their structure-function relationships. Fast SR-microCT imaging enabled the deformation behaviour to be captured with high temporal and spatial resolution. Time-resolved DVC highlighted the relationship between local strains and damage initiation and progression in the different biostructures undergoing plastic deformation, bending and/or buckling of their main microstructural elements. The results showed that SR-microCT continuous mechanical testing complemented and enhanced the information obtained from time-lapsed testing, which may underestimate the 3D strain magnitudes as a result of the stress relaxation occurring in between steps before image acquisition in porous biomaterials. Altogether, the findings of this study highlight the importance of time-resolved *in situ* experiments to fully characterise the time-dependent mechanical behaviour of biological tissues and biomaterials and to further explore their micromechanics under physiologically relevant conditions.

Keywords: Bone, time-resolved SR-microCT, continuous *in situ* mechanics, digital volume correlation, time-dependent behaviour.

1. Introduction

Biological materials, such as bone, as well as novel synthetic bioinspired foams and scaffolds, present complex heterogeneous, anisotropic and hierarchical structures [1–5]. Therefore, their mechanical behaviour is largely governed not only by their intrinsic material properties but also by their arrangement and distribution at different length scales [6–12]. At the mesoscale, trabecular and cortical bone mechanics mostly depend on the mineral density distribution and microarchitecture (i.e. porosity, orientation)[13–15], and thus a thorough characterization of the local mechanical properties at trabecular or osteonal level is needed in order to evaluate the effect of altered bone microstructure due to different musculoskeletal pathologies, such as osteoporosis or bone cancer, on the risk of fracture or the outcome of treatments and therapies [16–18]. On the other hand, engineered biomaterials are under constant development aiming to replicate the mechanical behaviour and morphology of bone by either acting as bone surrogates to evaluate the performance of medical implants and devices [19,20] or as scaffolds to treat critical-sized defects following disease or trauma [21]. Either way, these biostructures need to provide appropriate mechanical integrity both as a whole construct and locally to ensure a successful outcome. A deep understanding on the relationships between complex three-dimensional (3D) microstructures and local mechanics in bone and biostructures is, therefore, essential.

To date, the only experimental technique that allows for 3D local strain measurements within bone and biostructures is digital volume correlation (DVC) based on 3D imaging techniques such as X-ray micro-computed tomography (microCT) and concomitant *in situ* mechanics. Indeed, high-resolution microCT remains the main imaging modality used in the development of DVC [22–24], and it has been widely used to study the deformation of hard and soft biological tissues [25–29], as well as complex bone-biomaterial systems [30,31]. Traditionally, *in situ* microCT mechanical testing is performed in a stepwise manner, also known as time-lapsed testing, where loading is applied to the structures in discrete steps, each followed by a full tomographic acquisition after stress relaxation is stabilised [32,33]. However, all biomaterials exhibit a time-dependent mechanical behaviour which, in living tissues, plays a critical role in physiological activities [34]. Bone, for example, is a well-known viscoelastic tissue that exhibits frequency-dependent damping, stress relaxation and creep behaviour even at small load levels [35–38]. Therefore, DVC analysis based on time-lapsed tests cannot be used to capture the physiological strain mechanisms in biological materials, as their time-dependent response may alter the local measured strains. Thus, it is necessary to simultaneously measure local mechanical properties and directly quantify microstructural evolution with time in order to assess the dynamic deformation of bone and biomaterials.

In situ experiments performed in conventional laboratory-based microCT systems usually require long times for high-resolution image acquisition, hence time-lapsed testing remains the most viable procedure [39,40]. Although new systems and protocols are being developed providing higher temporal and spatial resolution microCT imaging in lab-based facilities [41–44], their application is certainly new, and the limited X-ray flux produced by micro-focused X-ray tubes demands an acceptable trade-off between noise and motion blurring when following a dynamic process [40,41]. Despite those disadvantages, Kytýř et al. [42] operated an in-house microCT system to investigate the deformation of porous hydrogel-based scaffolds during continuous *in situ* compression using DVC. However, the achieved spatial and temporal resolution were limited to ~30 μm and 120 s, respectively, and thus uniaxial compression was carried out at a considerably low loading rate of 0.4 μm / s to minimise motion artefacts [42]. On the other hand, the high flux of synchrotron X-ray radiation enables microCT images to be acquired with high signal-to-noise ratio (SNR) at high temporal and spatial resolution, and consequently, it allows the characterization of dynamic processes within 3D microstructures [45–47]. As such, time-resolved synchrotron experiments have been carried out over the past years to investigate the *in situ* sintering of ceramic materials [47–49], the underlying physics of lased additive manufacturing process [50] as well as the deformation of semi-solid metals subjected to uniaxial compression [51–53] and indentation [54] among other applications. To such extent, Cai et al. [52,54] made use of DVC to quantify the strain localization in a semi-solid alloy during continuous *in situ* SR-microCT compression [52] and indentation [54] with full tomographic datasets acquired in 4 and 9 s, and at 12.2 and 4 μm resolution, respectively, allowing the identification of dilatant shear bands during real-time compression and plastic deformation as well as compaction of individual grains during indentation. More recently, Peña Fernández et al. [55] explored the use of continuous *in situ* SR-microCT mechanics and DVC to investigate the effect of damage accumulation due to cyclic loading on the overall fracture outcome of cortical bone specimens, showing a decrease of the strain magnitudes prior to failure with the number of applied cycles. However, only the post-cyclic failure behaviour of cortical bone was evaluated, but a full characterisation of the structure-function relationships during the dynamic deformation of intact bone and biomaterials under mechanical loads was not addressed.

Therefore, the main aim of this study was to investigate, for the first time, the time-resolved deformation of a variety of bone structures (trabecular and cortical bone as well as cuttlebone) and analogues (synthetic foams and Mg-based scaffolds), using continuous *in situ* SR-microCT with uniaxial compression and DVC. The SR-microCT imaging acquisition parameters were fine-tuned for each biostructure allowing resolution of their main features of interest, and a comparison of the local DVC-computed strain fields based on SR-microCT

images acquired under both continuous and time-lapsed loading was carried out on the synthetic bone surrogates, due to their overall consistency in mechanical behaviour. Finally, the dynamic full-field strain distribution in all biostructures was evaluated over time in relation to, or as a joint contribution of, their microstructural changes and associated to damage initiation and propagation. The findings of this article will be of fundamental importance in establishing new guidelines for *in situ* time-resolved SR-microCT experiments of biomaterials, particular those showing high viscoelasticity and time-dependent mechanical behaviour.

2. Materials and methods

2.1. Specimens

A variety of materials, both synthetic and biological, were sourced to investigate the capability of the method in capturing the time-resolved deformation of biostructures with diverse morphology (Figure 1). This included synthetic foams, Mg-based open porous scaffolds, bovine trabecular and cortical bone as well as cuttlebone.
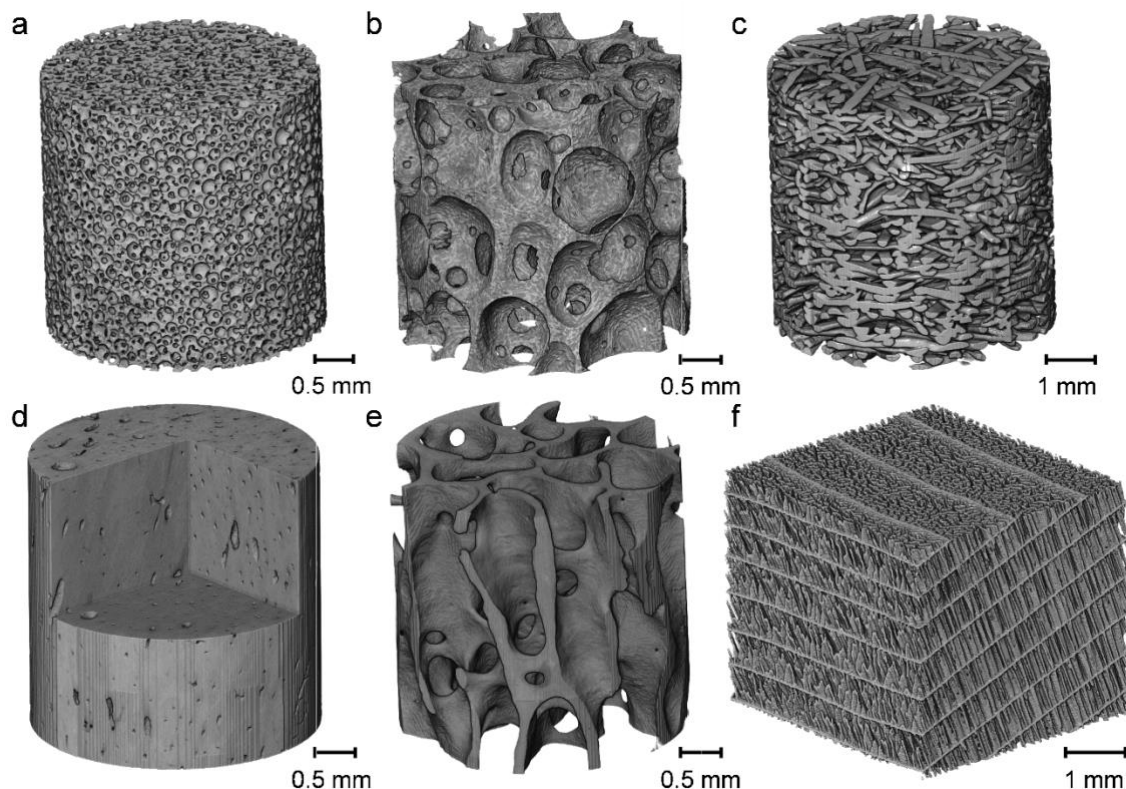

Figure 1. Reconstructed SR-microCT volumes of the specimens tested. (a) Closed-cell foam (Sawbones PCF20), (b) open-cell foam (Sawbones PCF15), (c) Mg-based open porous scaffold (d) cortical bone, (e) trabecular bone and (f) cuttlebone. SR-microCT images were acquired with a (a, b, d, e) 6.5 μm, (c) 10.4 μm and (e) 5.2 μm isotropic voxel size.

2.1.1. Synthetic foams

Closed-cell and open-cell foams (PCF20 and PCF15, Sawbones, Pacific Research Laboratories, WA, USA) were selected to represent bone microstructure with controlled mechanical and morphological properties. Cylindrical samples (6 mm diameter, 16 mm length) were extracted from Sawbones blocks (n = 6 per group) with a carbons steel drill bit and mounted on brass endcaps to achieve a final free length of 12 mm (2:1 aspect ratio), reducing experimental artefacts during mechanical testing [56].

2.1.2. Mg-based scaffolds.

Mg-based open porous scaffolds (Biotrics Bioimplants AG, Berlin, Germany) produced by liquid-phase sintering and designed for bone replacement were also investigated [4]. This material was of interest due to its higher ductility but similar strut thickness to trabecular bone. Furthermore, being a non-biological material, any possible radiation-induced damage can be neglected [57,58]. Cylindrical samples (n = 3, 8 mm diameter, 20 mm length) were embedded into acetal endcaps to achieve a 10 mm final free length and to ensure perpendicularity between the scaffold's main axis and base.

2.1.3. Trabecular and cortical bone.

Trabecular and cortical bone specimens were obtained from a fresh-frozen bovine tibial condyle and mid femoral diaphysis, respectively. Cylindrical plugs (6 mm for trabecular and 4 mm diameter for cortical bone, ~ 20 mm length) were cored in the proximal-distal direction using a trephine blur drill under constant water irrigation. The ends of the specimens were then trimmed plane and parallel with a bandsaw to achieve 14 mm length for trabecular and 10 mm length for cortical bone. All specimens were wrapped in gauze, soaked in phosphate buffered saline (PBS) and stored at −20°C until testing. Prior to the experiment, the ends of the specimens were cleaned, dried and embedded into brass endcaps using a custom-made alignment jig, achieving a nominal final free length of 12 mm and 8 mm (2:1 ratio) for trabecular and cortical bone, respectively [56].

2.1.4. Cuttlebone

Fresh specimens of *Sepia officinalis* Linnaeus, 1758, were acquired commercially from around the UK coastline and stored at -20°C. Several days prior to imaging, the cuttlebone was dissected from the organism, immersed in PBS, and stored in an airtight container. Several hours prior to imaging the cuttlebone was sectioned using a handheld rotary cutting disk into smaller cubic samples (approximately 5 x 5 x 5 mm) taken from near the central region of the cuttlebone, not including any of the dorsal shield material, and allowed to dry prior to testing.

2.2. Image acquisition.

SR-microCT was performed at the Diamond-Manchester Imaging Branchline I13-2 [59] of Diamond Light Source, UK. A partially coherent polychromatic 'pink' beam (8–30 keV) of parallel geometry was generated by an undulator from an electron storage ring of 3.0 GeV. The undulator gap was set to 5 mm for data collection and, to limit bone damage, 11 mm for low-dose alignment. The beam was reflected from the platinum stripe of a grazing-incidence focusing mirror and high-pass filtered with 1.4 mm pyrolytic graphite, 3.2 mm aluminium and 60 µm steel. Images were recorded by a sCMOS (2560 × 2160 pixels) pco.edge 5.5 (PCO AG, Germany) detector which was coupled to a visual light microscope with various objective lenses; 500 µm thick $CdWO_4$ and LuAG:Ce scintillators were used with the 1.25x and 2x objective lenses, respectively, leading to a field of view of 6.7 x 5.6 mm for the 1.25x lens and 4.2 x 3.5 mm for the 2x lens. On-chip pixel binning was used to improve the signal-to-noise ratio and facilitate faster framerates. Imaging settings were optimised for each specimen type and are summarized in Table 1.

Table 1. Summary of imaging settings used for the acquisition of SR-microCT images for each material type, including closed-cell (PCF20) and open-cell (PCF15) polyurethane foam, Mg-based open porous scaffold (Mg), trabecular bone (TB), cortical bone (CB) and cuttlebone (CF, cuttlefish bone). n: number of specimens tested per material type.

Material	n	Lens	Binning	Nominal voxel size (µm)	Projections	Exposure time (ms)	Read-out time (ms)
PCF20	6	2×	4	6.5	1201	9	2
PCF15	6	2×	4	6.5	1201	9	2
Mg	3	1.25×	4	10.4	1441	8	4
TB	5	2×	4	6.5	1201	15	3.5
CB	4	2×	4	6.5	1201	10	3.5
CF	1	1.25×	2	5.2	1201	10	2

Projection images were acquired over 180° of continuous rotation ('fly scan'). The compression rig was not moved between scans. The average delay between two sequential scans was approximately 11 s, as estimated from the timestamps of the generated files. Prior to reconstruction, the projection images were flat- and dark-field corrected. For each specimen, 40 flat- and dark-field images were collected before and after the scan series, to account for possible variations during the experiment. Flat-field images were collected with the compression rig in place, but the specimen absent. A filtered back projection algorithm

was used for reconstruction of the 3D datasets in Savu [60,61], which incorporated a fast ring artefact suppression algorithm based on the work of Titarenko et al. [62] and zingers removal. The specific plugins and parameters used during reconstruction are specified in Table S1.

For trabecular and cortical bone specimens, the radiation dose was estimated as in [58], assuming the same photon energy and flux (28.93 keV and 4.9×10^{13} photons/s, as estimated using SPECTRA code [63]). Specimens were considered as homogeneous cylinders with apparent densities of 0.55 g/cm^3 for trabecular [64] and 1.92 g/cm^3 for cortical bone [65]. A mass attenuation coefficient of 1.53 cm^2/g [66] was used for both cortical and trabecular bone, as it was previously shown to describe well the absorption profile simulated in the same experimental setup using FLUKA Monte Carlo [58]. This resulted in an estimated dose rate of 34.81 Gy/s and 45.27 Gy/s for cortical and trabecular bone specimens, respectively. The total radiation dose absorbed for each specimen is specified in Table S2, and it remained below 20.1 kGy for all specimens. The cuttlebone was tested in a different setup (i.e., loading stage), thus an estimation of the absorbed dose could not be conducted with the available data.

2.3. *In situ* mechanics.

In situ uniaxial compression testing was performed via a micro-mechanical testing device equipped with a 5kN load cell (CT5000, Deben Ltd, UK) on all specimens but the cuttlefish bone, which was tested in a 500 N load cell device (CT500, Deben Ltd, UK). Synthetic bone models, trabecular and cortical bone were placed within an environmental chamber and immersed in PBS solution throughout the duration of the test, whereas Mg-based scaffolds and cuttlebone were tested in dry conditions. All tests were carried out under displacement control at a constant crosshead speed of 0.1 mm/min. The total amount of compression for each specimen during a full tomogram acquisition is reported in Table S3.

For all specimens, a small preload (~2 - 10 N) was first applied to ensure good end contact prior to testing and two repeated tomographic datasets were acquired for DVC error analysis [24]. Synthetic bone models were divided into two groups (n = 3 per type/group) to allow a direct comparison of the deformation in the specimens during time-lapsed or continuous test. Half of the synthetic bone models were subjected to time-lapsed *in situ* mechanics at three compression levels (1%, 2% and 3% apparent strain). At each step, specimens were allowed to settle for 10 minutes before image acquisition to reduce stress relaxation during imaging, and full tomographic datasets were then acquired under the applied compression. Continuous loading was performed in all other specimens at a constant speed of 0.1 mm/min, with images acquired uninterruptedly during compression up to apparent failure (i.e., structural collapse or high densification). Therefore, the total number of full consecutive tomographic datasets collected was specimen dependent and are reported in Table S3.

2.4. Image postprocessing.

Following image acquisition and reconstruction, the 3D SR-microCT images for each specimen were rigidly registered using the first preloaded image as a reference [23]. Registration was performed with dedicated Matlab (v2018a, MathWorks, Natick, MA, USA) scripts. Prior to registration, images were converted from 32-bit to 16-bit. Mattes mutual information algorithm [67] was used as a similarity metric and one-plus-one evolutionary configuration [68] was employed for optimising the image metric, with an initial and minimum size of the search radius of 10^{-5} and 1.5×10^{-6}, respectively, a growth factor of the search radius of 1.05, and a maximum number of iterations of 100. After rigid alignment of the 3D datasets, images were denoised in Matlab using an anisotropic diffusion filter, where the gradient threshold and number of iterations were estimated using Matlab in-built function *imdifussest* on the centre-slice of each specimen [69,70]. Finally, a volume of interest (VOI) was selected for each specimen as the volume of material present on both the first and last acquired tomograms.

The filtered images were segmented using the pixel classification workflow available in ilastik (V1.3.0) [71]. For each specimen, six scans were selected, and the central 20 slices were used to train the classifier and segment each volumetric image into two classes (i.e., solid materials and background). The model was trained computing different features (i.e., Gaussian smoothing, Laplacian of Gaussian, Gaussian Gradient Magnitude, Difference of Gaussians, Structure Tensor Eigenvalues and Hessian of Gaussian Eigenvalues) in 3D at five σ values (σ = 0.3, 0.7, 1.0, 1.6, 3.5) and in 2D with σ = 5.0. The segmented images of the first acquired dataset (i.e., preload configuration) for each specimen was used for a morphological analysis. The solid volume fraction (SV_f) was computed for each specimen as the volume of solid material over the entire VOI. Additionally, mean strut thickness and spacing in synthetic bone models, mean fibre thickness and spacing in Mg-based scaffolds, mean trabecular thickness and spacing in trabecular bone specimens, mean canal thickness and spacing in cortical bone specimens and mean pillar thickness and spacing in cuttlebone chamber were computed using BoneJ [72] plugin in FIJI [73]. For Mg-based scaffolds, the evolution of the fibre spacing during compression was also analysed.

2.5. Digital volume correlation (DVC).

DVC (DaVis v10.05, LaVision, Germany) analysis was performed to evaluate the 3D full-field strains of all specimens and quantify their dynamic deformation. The DaVis software is based on a local approach of deformable registration and further details on the operating principles of the algorithm are detailed elsewhere [74,75]. Briefly, the measurement volumes (i.e., 3D image) are divided into smaller subvolumes and the matching between the reference and

deformed images is achieved via a direct cross-correlation function of the gray-levels, which is preceded by a Fast Fourier Transform (FFT)-based correlation to initialise the computation. The DaVis software adopts a multipass scheme that uses the displacement gradient from a previous pass to deform the subvolume on the subsequent pass until the highest possible correlation is achieved.

The acquired preloaded repeated scans were used to evaluate displacement precision and strain uncertainties (i.e., mean absolute strain error (MAER) and standard deviation of the error (SDER), also known as accuracy and precision, respectively) [76] using ten different multipass schemes with final subvolumes ranging from 8 to 80 voxels (see Table S5, Fig S1, S2). No overlap between subvolumes was used, meaning each subvolume did not share any gray-scale pattern with their neighbouring one in the correlation procedure. The final DVC-schemes used for each material and the corresponding displacement and strain errors are summarized in Table 2. Such schemes then allowed to evaluate the 3D full-field strain distribution in the specimens over time (i.e., four-dimensional (4D) evaluation) in relation to the deformation induced by the compressive applied load.

Table 2. Summary of DVC multipass scheme used for each material and corresponding displacement and strain errors for the n number of specimens analysed for closed-cell (PCF20) and open-cell (PCF15) polyurethane foam, Mg-based open porous scaffold (Mg), trabecular bone (TB), cortical bone (CB) and cuttlebone (CF, cuttlefish bone). Errors are reported as mean (standard deviation) for both MAER and SDER among the n specimens per material.

Material	n	DVC multipass scheme (voxel)	Subvolume size (µm)	Displacement precision (µm)[b]	MAER (µε)	SDER (µε)
PCF20	6	128[a]-64-56-48-40	260.0	0.49 (0.44)	259 (160)	81 (35)
PCF15	6	128[a]-64-56-48-40	260.0	0.57 (0.28)	271 (116)	112 (40)
Mg	3	160[a]-80-72-64-56	364.0	1.01 (0.55)	540 (306)	284 (234)
TB	5	144[a]-72-64-56-48	312.0	1.04 (0.49)	499 (174)	177 (95)
CB	4	144[a]-72-64-56-48	312.0	0.82 (0.33)	347 (95)	134 (26)
CF	1	96[a]-48-40-32-24	124.8	0.46	225	62

[a] FFT pre-shift windows size preceding multi-pass direct correlation DVC computation.

3. Results

The sourced materials used in this study presented a clearly characteristic microstructure (Figure 1) as highlighted by the morphological analysis (Table 3), with solid volume fractions ranging from 16.9% for the cuttlebone to 96.9% in cortical bone specimens, the most and least porous specimen, respectively. The non-biological materials (i.e., PCF15, PCF20 and Mg specimens) showed a smaller intra-specimen variation in all the measured morphometric parameters compared to trabecular and cortical bone specimens. Synthetic bone models exhibited comparable porosity to trabecular bone specimen. The thinnest analysed structures corresponded to the 25.7 µm-thick pillars in the cuttlebone chamber, 42.5 µm-thick walls in the closed-cell foam PCF20 and 83.6 µm-thick canals in cortical bone specimens. Trabecular bone, open-cell foam PCF15 and Mg-scaffolds displayed a similar thickness.

Table 3. Summary of the morphological parameters of the analysed biostructures including closed-cell (PCF20) and open-cell (PCF15) polyurethane foam, Mg-based open porous scaffold (Mg), trabecular bone (TB), cortical bone (CB) and cuttlebone (CF, cuttlefish bone). For each material, solid volume fraction (SV_f), thickness and spacing are reported as mean (standard deviation) among the n specimens per material.

Material	n	SV_f (%)	Thickness (µm)	Spacing (µm)
PCF20	6	26.4 (1.1)	42.5 (1.4)	170.8 (4.9)
PCF15	6	22.8 (1.4)	139.9 (4.5)	741.6 (60.1)
Mg	3	42.8 (1.0)	143.7 (1.2)	220.0 (8.3)
TB	5	21.7 (6.3)	179.0 (35.7)	654.3 (33.9)
CB	4	96.9 (0.3)	83.6 (15.8)[a]	323.9 (43.7)[a]
CF	1	16.9	25.7	101.4

[a] Thickness and spacing of cortical bone Harversian and Volkmann canals.

The optimisation of the imaging settings allowed to resolve the main features of interest in each material for both static and dynamic conditions (Figure 2-I,II). A qualitative inspection of the SR-microCT images demonstrated that the smallest details in the biostructures, such as the structural fillers in the open-cell foam (PCF15), the thinnest vascular canals in cortical

bone and the pillars in the cuttlebone, were not affected by motion artefacts during dynamic imaging (Figure 2-II) with the exception of regions where failure occurred due to the applied compression (Figure 2-III). This was also observed as a small shift in the image histograms (Figure 2-IV), and it was more evident for the cellular foam (PCF15), for which the contrast between the fillers and matrix was partially lost (Figure 2a-III,IV).
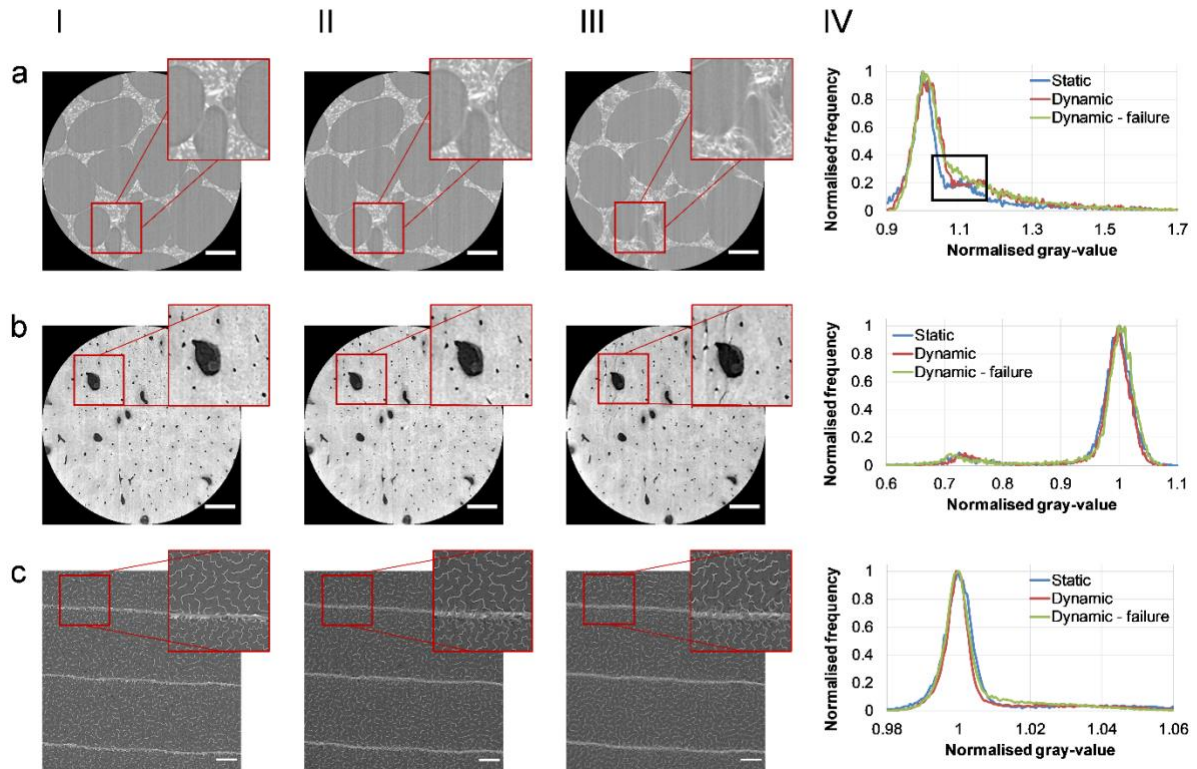

Figure 2. Analysis of SR-microCT images acquired during static and dynamic conditions. A representative SR-microCT cross-section is shown for (a) open-cell foam PCF15, (b) cortical bone and (c) cuttlebone while imaging was performed statically (I), and dynamically during the linear loading regime (II) and mechanical failure (III). (IV) Normalised histograms of the zoomed-in regions in (I-III). Normalisation was performed with respect to the mode (e.g., most frequent) values of each histogram. Scale bars: 500 µm.

The apparent mechanical behaviour of the closed-cell foam (PCF20) was fairly consistent for all specimens, showing an initial elastic range up to ~2-3% deformation followed by strain hardening period in which pores started to collapse (Figure 3a). Stress-relaxation was visible for specimens subjected to time-lapsed compression at the end of each step, when the actuator was stopped, and specimens were allowed to settle before image acquisition. DVC-computed third principal strains (i.e., ε_{p3}) increased linearly with the applied compression, with specimens tested dynamically experiencing approximately two-fold local strain in average (Figure 3b). The 3D full-field ε_{p3} revealed local strain accumulation in the centre of the specimens, as the pores in the solid foam matrix closed due to the applied deformation (Figure 3c). Off-axis compression was detected in PCF20#2 and PCF20#6, which showed maximum

strain levels accumulating on one side of the volume and higher heterogeneity in the strain distribution at each step (Figure 3b, Video S1,S2).
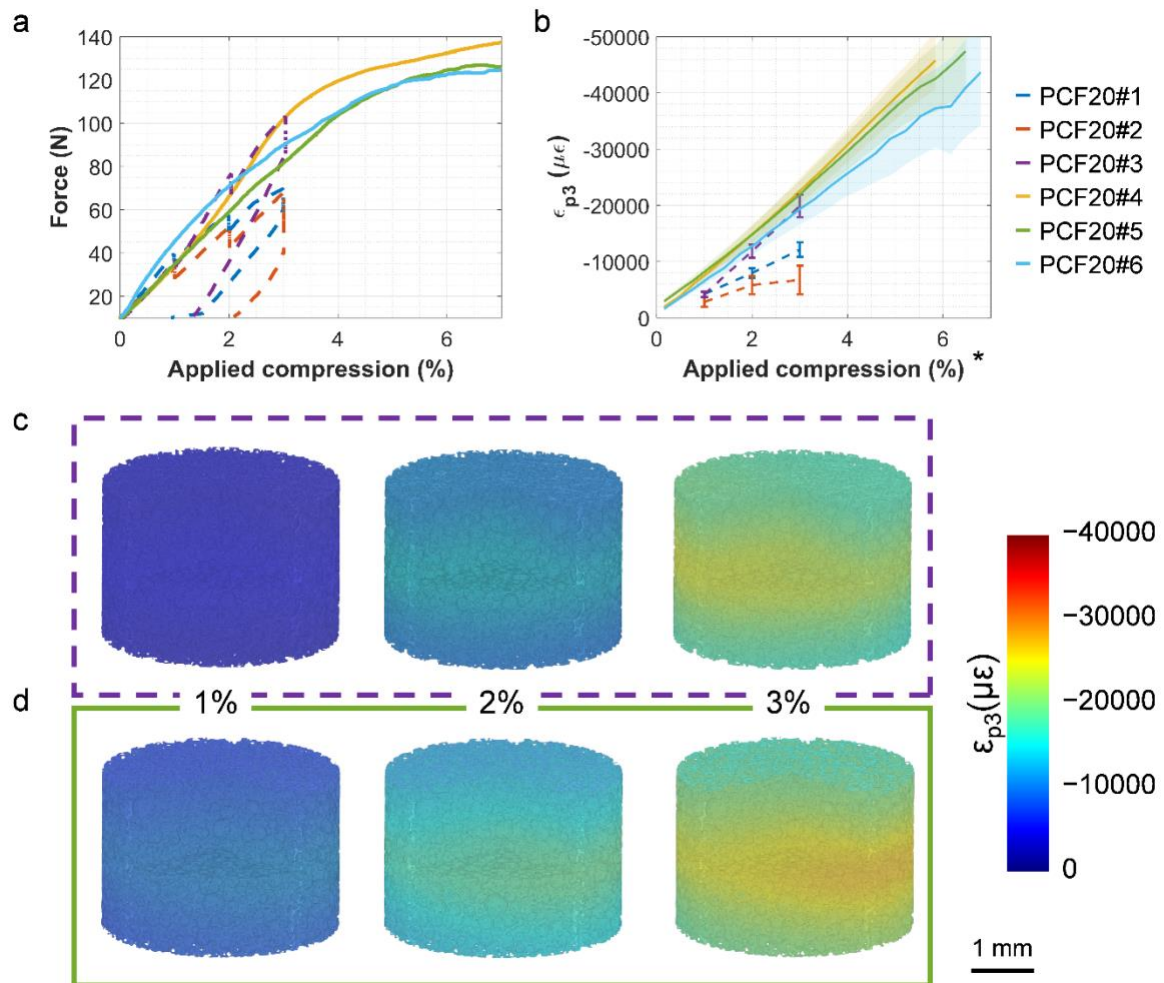

Figure 3. *In situ* SR-microCT compression of PCF20 closed-cell foams subjected to time-lapsed (#1-3) or continuous (#4-6) compression. (a) Force-compression curves for the six specimens. For specimens #1 to #3 the force shows a drop at the end of each compression step, corresponding to the time the specimens were allowed to settle prior to SR-microCT imaging; unloading part of the curve after 3% compression is also shown. (b) DVC-computed minimum principal strains (ε_{p3}) at each step (i.e., following each acquired tomogram) in relation to the applied deformation. The solid-dashed lines represent the mean ε_{p3} values, with the shaded areas and error bars representing the standard deviation over the entire specimen volume. The 3D full-field third principal strain distribution (ε_{p3}) at 1%, 2% and 3% applied compression is visualised for (c) PCF20#3 and (d) PCF20#5 specimens, with specimen-dependent colour-coded bounding boxes as in (a) and (b). The 4D strain distribution for all specimens can be found in Videos S1 and S2. *The applied compression for the specimens imaged dynamically was estimated from the actuator speed, imaging time and delay between each pair of consecutive tomograms.

Cellular open foam specimens (PCF15) displayed a linear monotonic trend up to ~1% compression at apparent level, with yielding occurring between 1.5% to 2% compression (Figure 4a). The linear elastic behaviour was followed by a significant hardening period (up to 3-4% compression), then by a prolonged softening and strength reduction. Unlike the closed-

cell foam, open-cell foams experienced structural failure, which was identified as a drop in the force at apparent level (Figure 4a) and a decrease in the mean local ε_{p3} (Figure 4b). The specimens tested dynamically showed higher local ε_{p3} levels before yielding compared to those tested in a time-lapsed manner, with the exception of PCF15#4, in which the strain distribution showed higher variation before yielding (Figure 4b, Video S2). The 3D ε_{p3} distribution was highly heterogeneous for all specimens, with maximum local strain accumulating in specific regions (Figure 4c, Video S3, S4), which eventually led to local failure in the specimens tested dynamically, followed by a strain redistribution in the structure (Figure 4b, Video S4, white arrows). The acquisition of SR-microCT images in a continuous fashion during compression allowed to track the evolution of such local strain accumulation leading to failure at high spatial and temporal resolution, and it is demonstrated for specimen PCF15#6 (Figure 5). It could be observed how strain built-up around specific thin walls that collapsed when local compressive strains exceeded 30,000 $\mu\varepsilon$ (Figure 5, Steps 4-5). Following the first failure and crack development, local strain released from that walls and accumulated in a different region, which also collapsed when for $\varepsilon_{p3} < -30,000$ $\mu\varepsilon$ (Figure 5, Steps 5-7).
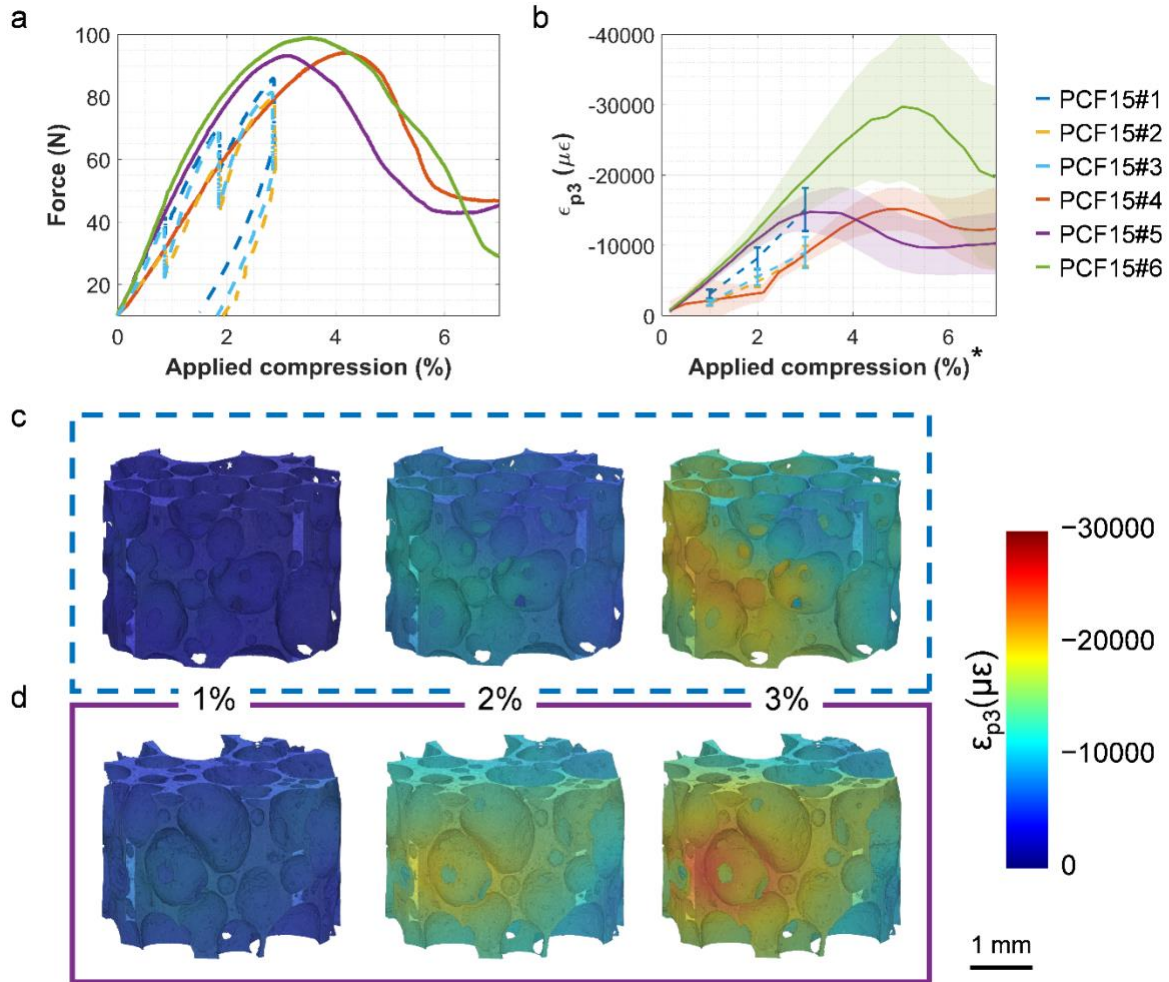
Figure 4. *In situ* SR-microCT compression of PCF15 cellular open foams subjected to time-lapsed (#1-3) or continuous (#4-6) compression. (a) Force-compression curves for the six specimens. For specimens #1 to #3 the force shows a drop at the end of each compression step, corresponding to the time the specimens were allowed to settle prior to SR-microCT imaging; unloading part of the curve after 3% compression is also shown. (b) DVC-computed minimum principal strains (ε_{p3}) at each step (i.e., following each acquired tomogram) in relation to the applied deformation. The solid-dashed lines represent the mean ε_{p3} values, with the shaded areas and error bars representing the standard deviation over the entire specimen volume. The 3D full-field third principal strain distribution (ε_{p3}) at 1%, 2% and 3% applied compression is visualised for (c) PCF15#1 and (d) PCF15#5 specimens, with specimen-dependent colour-coded bounding boxes as in (a) and (b). The 4D strain distribution for all specimens can be found in Videos S3 and S4. *The applied compression for the specimens imaged dynamically was estimated from the actuator speed, imaging time and delay between each pair of consecutive tomograms.
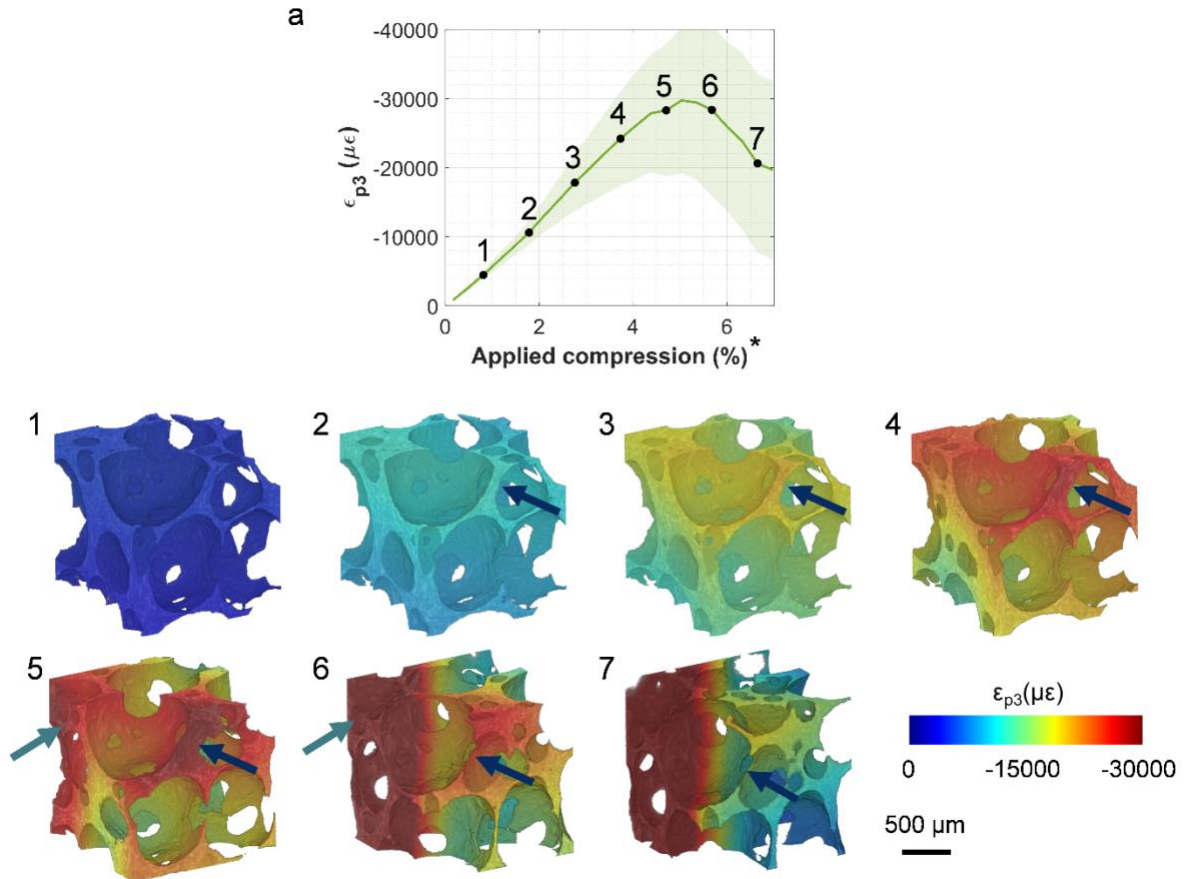
Figure 5. Local failure tracking in a region of interest of PCF15#6. The 3D full-field third principal strain distribution (ε_{p3}) at the selected time-points in (a) are represented. Arrows indicate regions of maximum local strains where failure occurred, with blue arrows indicating the first failure event and green arrows the next collapsed regions.

Mg-based porous scaffolds displayed a highly similar mechanical behaviour to closed-cell foams both at apparent and local level (Figure 6) with force-compression curves showing an elastoplastic response. Initially, scaffolds underwent liner elastic deformation until yielding (~1-2.5% deformation). As the load increased, a strain hardening region was observed, where the fibers started to plastically deform and pores to close leading to impingement of the fibers and consequent densification of the scaffolds (Figure 6). Local ε_{p3} increased approximately linear with the applied compression for all specimens, reaching mean values of about −50,000 µε at 10% compression and an average decrease of the fibre spacing above 7% (Figure 6b, c); however, the 4D distribution through the volume evidenced a more homogeneous compressive deformation in Mg#1 scaffold compared to Mg#2 and Mg#3, which experienced a localised lateral compression (Video S5). Thus, high local ε_{p3} values were identified in regions where fibers were most compressed and collapsed against adjacent ones, where the spacing between the fibers was reduced (Figure 6d, e).
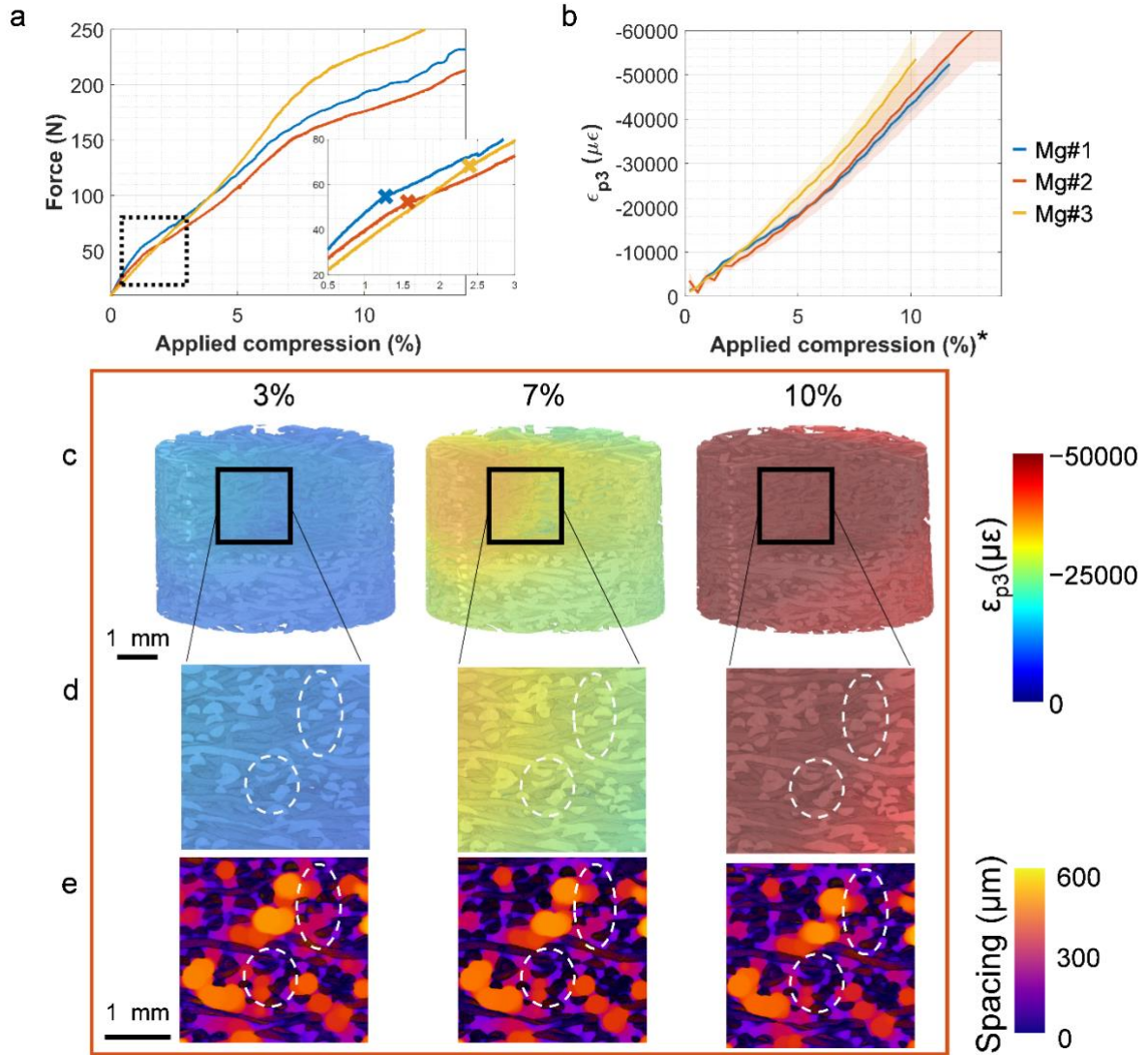
Figure 6. *In situ* SR-microCT compression of Mg-based scaffolds undergoing continuous compression. (a) Force-compression curves for the three specimens. (b) DVC-computed minimum principal strains (ε_{p3}) at each step (i.e., following each acquired tomogram) in relation to the applied deformation. The solid lines represent the mean ε_{p3} values, with the shaded areas representing the standard deviation over the entire specimen volume. The 3D full-field third principal strain distribution (ε_{p3}) at 3%, 7% and 10% compression are visualised for (c) the entire volume of Mg#2 specimen and (d) a magnified region of interest with white area indicating localised impingement of the fibers next to highly strained regions. (e) Colour-coded fibre spacing (i.e., negative space of the fibres) in the same region of interest of (d) with white ovals indicating pores closing. The 4D strain distribution for all specimens can be found in Video S5. *The applied compression was estimated from the actuator speed, imaging time and delay between each pair of consecutive tomograms.

The high heterogeneity in the microstructure of trabecular bone specimens led to a more variable mechanical behaviour under compression compared to the above reported synthetic materials (Figure 7). At an apparent level, force-compression curves showed an initial toe region due to the imperfections on the initial co-planarity of the two endcaps. Thereafter, all the specimens showed a monotonic trend that was linear until failure (Figure 7a). The ultimate

load correlated well with the bone volume fraction ($R^2 = 0.73$), with plate-like structures (TB#1 and TB#2) taking higher load before failure compared to rod-like structures (TB#3 and TB#4) and the mixed configuration of TB#5 specimen (Figure 7a, Video S6). Similarly, mean local ε_{p3} showed an increasing linear trend with the applied compression prior to failure, after which strains built-up more steeply due to the accumulation of cracks in the trabecular structure (Figure 7b, Video S6). Before cracks appeared, mean local ε_{p3} ranged between -10,000 µε to -15,000 µε (Figure 7b), however, the strain distribution was highly heterogeneous throughout the volume, with localised regions exceeding those values (Figure 7c, d). The 4D evaluation of the strain distribution demonstrated that maximum strain levels accumulated in regions where failure, in the form of cracks, later occurred (Figure 7c, d, Video S6). Additionally, the rod-like trabecular structure seemed to be able to sustain higher compressive strains before fracture (Figure 7c) compared to the plate-like structure (Figure 7d).

Figure 7. *In situ* SR-microCT compression of trabecular bone (TB) structures undergoing continuous compression. (a) Force-compression curves for the five tested specimens. (b) DVC-computed minimum principal strains (ε_{p3}) at each step (i.e., following each acquired tomogram) in relation to the applied deformation. The solid lines represent the mean ε_{p3} values, with the shaded areas representing the standard deviation over the entire specimen volume.

× symbols in the insert indicate step prior to cracking. The 3D full-field third principal strain distribution (ε_{p3}) before, during and after failure is visualised for (c) TB#4 (rod-like structure) and (d) TB#2 (plate-like structure) specimens, with specimen-dependent colour-coded bounding boxes as in (a) and (b). Arrows indicate highly strained regions tracked over time where cracks in the structure appeared. The 4D strain distribution for all specimens can be found in Video S6. *The applied compression was estimated from the actuator speed, imaging time and delay between each pair of consecutive tomograms.

Similar to trabecular bone, the mechanical behaviour of cortical bone showed noticeable intra-specimen differences (Figure 8). All specimens also displayed an initial toe region in the force-compression curves, followed by a monotonic linear trend up to failure (Figure 8a). Unlike trabecular bone, the differences in the apparent mechanical behaviour, both stiffness and load to failure, were not related to the microstructure but rather to the off-axis compression and consequent tilting of specimens CB#1 and CB#3 during compression (Video S7). Prior to failure, mean local ε_{p3} showed a mostly uniform distribution with a linear increase (Figure 8b). Additionally, local strains accumulated in regions where longitudinal cracks, piercing the entire cortical volume, were observed after failure (Figure 8c, d). Such strains did not exceed −10,000 µε locally before crack development, with mean local ε_{p3} in the analysed volume ranging between −4,119 µε and −7,273 µε among the four specimens (Figure 8b, Video S7).
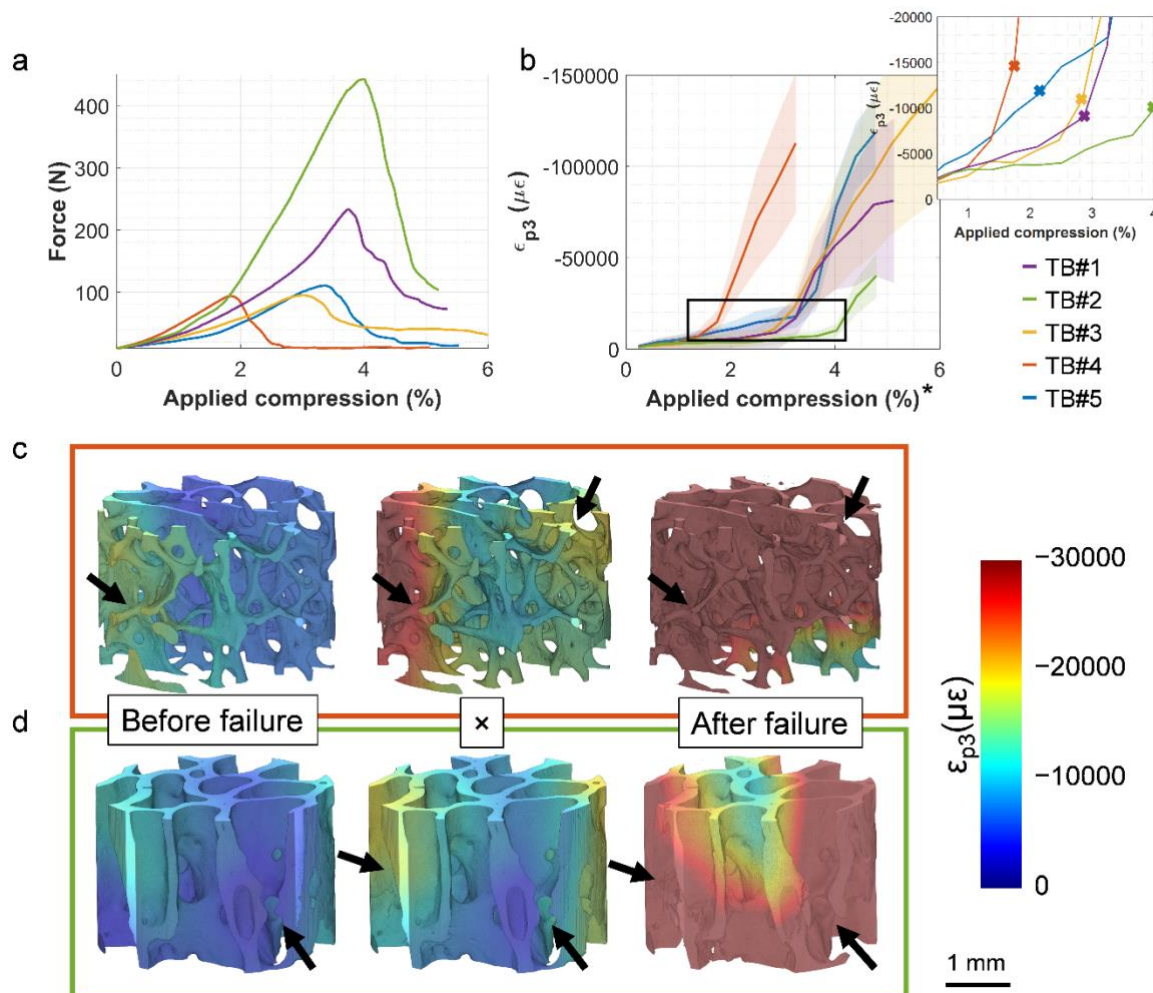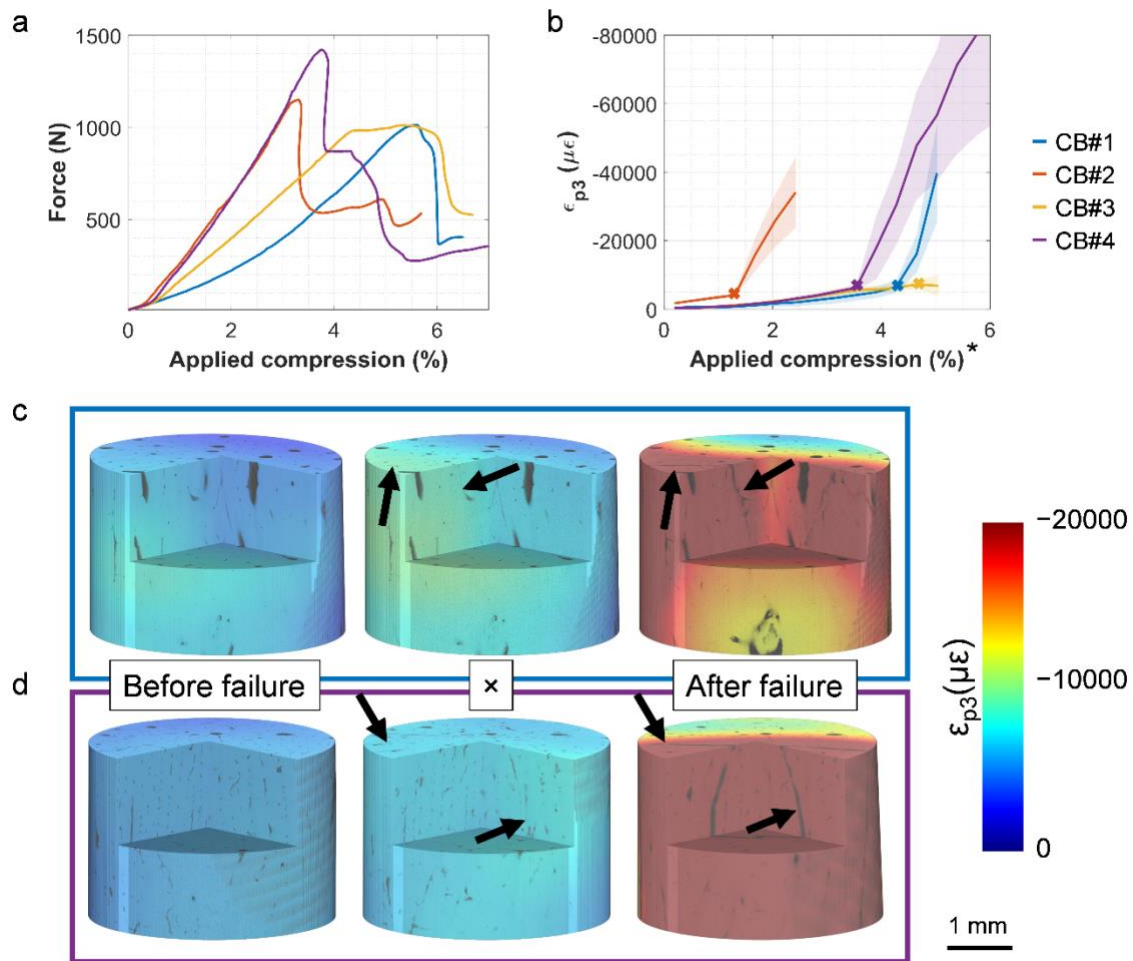
Figure 8. *In situ* SR-microCT compression of cortical bone (CB) structures undergoing continuous compression. (a) Force-compression curves for the four tested specimens. (b) DVC-computed minimum principal strains (ε_{p3}) at each step (i.e., following each acquired tomogram) in relation to the applied deformation. The solid lines represent the mean ε_{p3} values, with the shaded areas representing the standard deviation over the entire specimen volume. × symbols in the insert indicate step prior to cracking. The 3D full-field third principal strain distribution (ε_{p3}) before, during and after failure is visualised for (c) CB#1 and (d) CB#4 specimens, with specimen-dependent colour-coded bounding boxes as in (a) and (b). Arrows indicate highly strained regions tracked over time where cracks in the structure appeared. The 4D strain distribution for all specimens can be found in Video S7. *The applied compression was estimated from the actuator speed, imaging time and delay between each pair of consecutive tomograms.

Some cracks were found to initiate next to the Harversian canals and propagated through the structure by deviating among some osteons (Figure 9). The development of cracks in the specimens resulted in a more heterogeneous strain distribution and a sudden increase in local ε_{p3}, with maximum strain values around the crack region exceeding −20,000 µε (Figure 8b, Video S7).
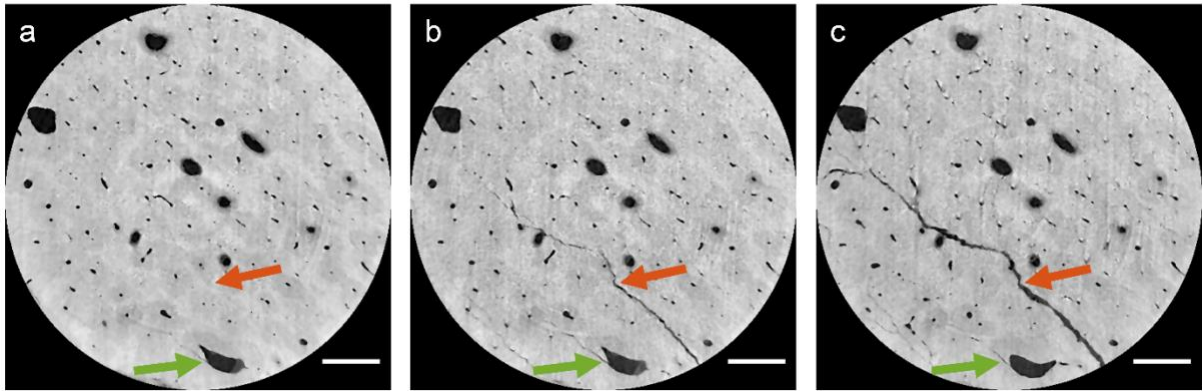
Figure 9. Crack initiation and propagation in CB#5 cortical bone specimen. (a) Some cracks initiated next to a Harversian canal (green arrow), in the more strained regions (Figure 8c). (b, c) Larger cracks promoting structural failure as a result of strain heterogeneity (Fig. 8d) showed a deviation among the osteons during propagation (orange arrow). Scale bars: 500 μm.

Force-compression curves for the cuttlebone specimen showed an initial linear region up to ~6% compression; then, yielding occurred and the pillars at the bottom started to collapse, which resulted in a drop in the force. Thereafter, a plateau was observed while the pillars were compressed followed by a second linear increase in the force up to ~18% compression, where a second layer of pillars failed and thus, the force dropped (Figure 10a). The full-field ε_{p3} distribution was highly heterogeneous in the analysed volume, with mean strains showing an irregular increasing trend (Figure 10b). Local ε_{p3} concentrations were found around the septa, which then transferred the load though the pillars (Figure 10c), leading to an intermittent strain accumulation when followed in 4D (Video S8). While the septa were able to withstand local compressive strains below -10,000 με without collapsing, the pillars seemed to fail at approximately −8,000 με, and maximum local ε_{p3} were then observed in the fracture region (Figure 9c).
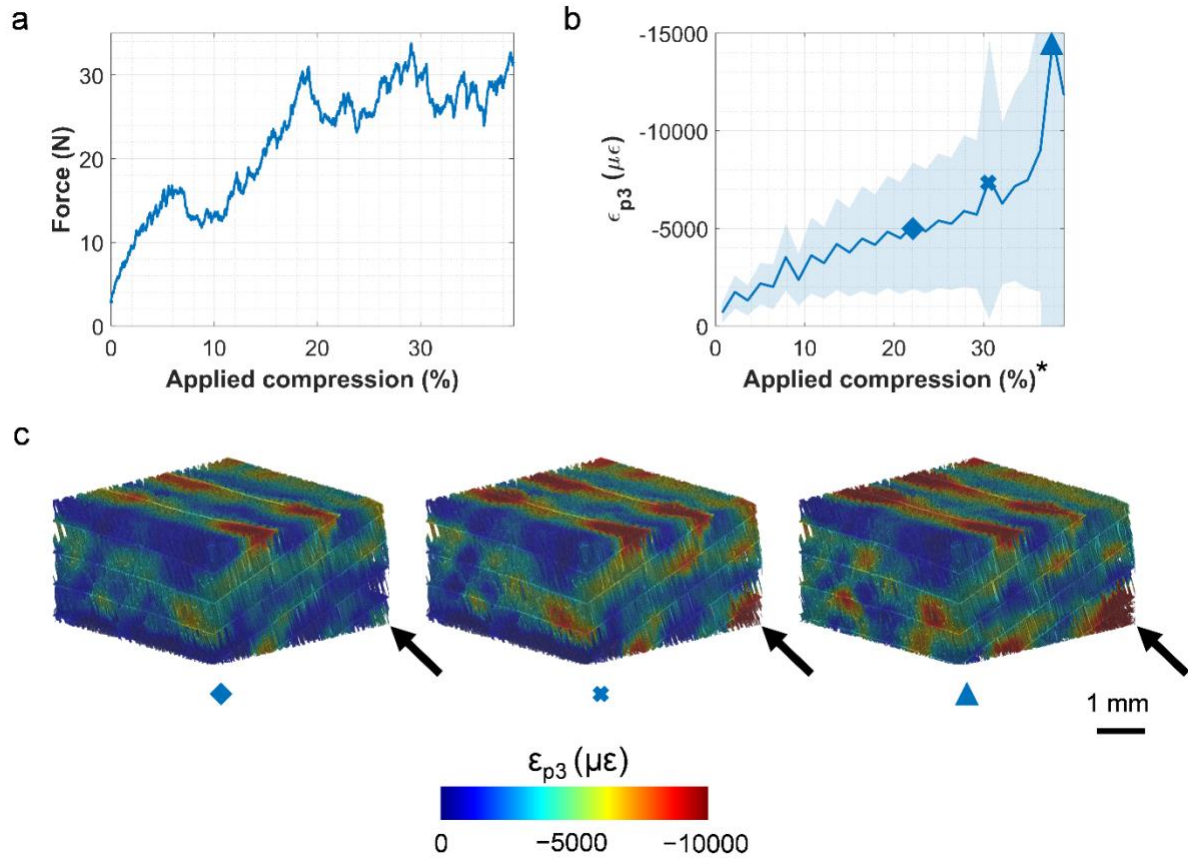
Figure 10. *In situ* SR-microCT compression of cuttlebone (CF) structure undergoing continuous compression. (a) Force-compression curves for the tested specimen. (b) DVC-computed minimum principal strains (ε_{p3}) at each step (i.e., following each acquired tomogram) in relation to the applied deformation. The solid lines represent the mean ε_{p3} values, with the shaded areas representing the standard deviation over the entire specimen volume. (c) The 3D full-field third principal strain distribution (ε_{p3}) at the compression levels denoted by the symbols. Arrows indicate highly strained regions tracked in the pillars over time where collapse was observed. The 4D strain distribution can be found in Video S8. *The applied compression was estimated from the actuator speed, imaging time and delay between each pair of consecutive tomograms.

4. Discussion

In this study, the four-dimensional (4D) deformation behaviour of biological and synthetic porous materials was investigated via *in situ* time-resolved synchrotron micro-computed tomography (SR-microCT) with uniaxial compression and digital volume correlation (DVC). Time-resolved tomographic imaging of the compressive deformation allowed the identification of damage initiation and progression, as well as the quantification of the full-field strain distribution and evolution in various biostructures, circumventing the characteristic stress-relaxation effects of porous viscoelastic materials subjected to time-lapsed mechanical testing.

The investigated porous materials herein presented included a wide range of microstructural features, thus allowing the assessment of the method for different material porosities, wall

thicknesses and pore sizes. The imaging settings were fine-tuned for each biostructure in order to minimise blurring and imaging artefacts during continuous deformation that could affect DVC computation. Features thinner than 50 μm, such as cuttlebone pillars and cortical bone canals (Figure 2, Table 3), were resolved both in static and dynamic conditions with high nominal (i.e., 5.6 to 10.4 μm effective voxel size) and temporal (i.e., 12 to 22.2 s per scan) resolution. All specimens were compressed at a displacement rate of 1.67 μm s^{-1} except the cuttlebone which used 3.33 μm s^{-1}, resulting in a total compression of 22 to 40 μm (i.e., 3 to 7 times the voxel size) per scan. Such a ratio of total compression over voxel size is in line with previous work on the semi-solid deformation of granular alloys using time-resolved *in situ* SR-microCT mechanics [51,52,54]. However, a qualitative and semi-quantitative comparison of the contrast and definition of the main features of interest in statically vs dynamically acquired images have not been previously reported. In this study, it was shown that the compression applied did not compromise image quality throughout the mechanical tests and only some blurring and distortion was observed in regions of structural failure (Figure 2) as such phenomena, particularly in the propagation stage, occur due to cracks developing at a faster rate than concomitant image acquisition.

A comparison between time-lapsed and continuous stress-strain curves has previously been assessed in aluminium foams and trabecular bone cylinders subjected to *in situ* microCT compression [32], showing no significant differences between the curves. However, to the authors' knowledge, comparison of time-lapsed versus continuous DVC-computed local strains has not been previously studied. Here, synthetic foams of different porosities were used to assess such differences due to their anisotropic and inhomogeneous nature, very similar to that of trabecular bone, but with highly reproducible microarchitecture and overall consistency in mechanical behaviour (Table 2). Similar to previous studies, the elastic part of the time-lapsed and continuous force-compression curves showed almost identical shapes, with a trend towards lower forces close to the yielding point in the time-lapsed test (Figure 3a, 4a). As a 10-min waiting period was imposed at the end of the application of each strain step in the time-lapsed compression test, the stress relaxation reached a plateau. This inherent relaxation was responsible for the lower measured forces in the yielding phase of the curve and in a local strain redistribution between steps (Figures 3, 4). As such, the full-field strain analysis of both time-lapsed and continuous test showed a comparable 3D distribution, yet lower strain magnitudes were observed in the time-lapsed test (Figures 3c, 4c). This was more important in the closed-cell foams PCF20, where local compressive strains following stress-relaxation were up to three-fold lower than during compression (Figure 3b). Although the comparison between time-lapsed and continuous testing was limited to only three compression steps due to experimental time and resources requirements, this seemed

sufficient to assess the linear elastic behaviour of synthetic foams as well as the elastic-plastic transition response of the material, thus, providing insight on the onset of damage initiation. Altogether, these results highlight the need for fast imaging during *in situ* microCT mechanical testing to capture the dynamic deformation behaviour of porous synthetic and biological materials, allowing to fully appreciate the strain-damage relationships.

Despite the porous nature of all the studied materials, the higher solid volume fraction and density of cortical bone specimens resulted in a more brittle failure when loaded in compression. On the other hand, the remaining biostructures, including synthetic biostructures, trabecular bone and cuttlebone, deformed by the elastic bending and buckling as well as the plastic collapse of their struts/walls when loaded. Both closed-cell PCF20 and open-porous Mg foams showed a ductile behaviour and the plastic deformation of their struts/fibers and closing of their pores in highly strained regions, resulting in a densification of the structure, which was more pronounced towards its centre due to the applied uniaxial compression (Figure 3c, 6c). On the other hand, the open cellular foam PCF15 and trabecular bone specimens displayed a more heterogeneous strain distribution, due to the elastic bending and buckling of the struts and trabeculae (Fig 4c, 7c, d). As such, strain accumulation was observed in specific walls and trabeculae undergoing higher deformation due to bending and buckling, which ultimately resulted in fracture and overall failure of the structure. Moreover, the acquisition of multiple microCT scans through the compression test also allowed to track the failure initiation and progression with high spatial and temporal resolution (Figure 5). While the accumulation of compressive strains led to fracture of the walls/trabeculae, overloading the structures beyond the primary failure point resulted in a strain release of the failed region coordinated with a strain build-up in another region (videos S4, S6). This strain release behaviour following failure in the form of cracks has been previously observed in trabecular bone and bone-biomaterial systems during time-lapsed *in situ* microCT compression [30], where the formation of microcracks caused the redistribution of compressive strains in the structure and an increase of tensile and shear strains in the failed regions. Interestingly, local compressive strains in the cuttlebone specimen displayed a continuous redistribution through the mechanical test in non-fractured regions, due to its distinctive microstructure, where the stiff and hard layers within the septa alternate with more compliant and ductile zones, possibly to direct failure to internal 'sacrificial' structures via chamber collapse, maintaining overall integrity and function of the cuttlebone as a buoyancy regulator [77]. Therefore, the septa bore higher compressive strains without structural failure, that were transferred to the different layers through the pillars (Video S8). More cuttlebone specimens will need to be tested in future studies to further understand the load and strain transfer ability of such a complex biostructure. Nevertheless, these preliminary results

demonstrate the ability of the method to capture the time-resolved deformation of the thin pillars and septa of cuttlebone material.

DVC based on *in situ* time-lapsed mechanical testing with microCT is increasingly gaining interest to quantify the 3D deformation mechanisms of bone at different length scales, from organ to tissue level [25,78]. Most studies focused on trabecular bone at the macro- [78] and mesoscale [30,79] due to its intrinsic microarchitecture, which provides a natural greyscale pattern for the DVC method [80]. However, the higher-spatial resolution achieved using SR-microCT have enabled the assessment of trabecular bone strains at tissue level and consequently, its relation to microdamage initiation and progression [57,58,81]. Despite the high-resolution images acquired in this study, with a nominal resolution of 6.5 µm , the coarse subvolumes used for the DVC analysis (i.e., 312 µm), did not allow to obtain strain measurements at tissue level but at the whole trabecular thickness level so to minimise the uncertainties of the method [24,82]. The continuous full-field strain analysis herein presented show similar strain patterns to those previously reported at a higher resolution using time-lapsed testing, but approximately two-fold increased strain magnitudes both before and after failure [81]. Interestingly, the mean DVC-computed strains following yielding but prior to failure ranged between −10,000 µε to −15,000 µε (Fig. 7b), which is in line with previously reported yielding strain values for human trabecular bone in compression (~ −10,000 µε [83,84]). Recently, Turunen et al. [85] reported sub-trabecular strain measurements using time-lapsed *in situ* high-resolution (i.e. 3.6 µm voxel size) SR-microCT mechanics, where subvolumes as small as 10 voxels were employed for the DVC analysis, resulting in a highly heterogeneous strain distribution within the trabecular bone tissue, and average volumetric strains up to 77,000 µε at the global yield point, prior to fracture, one order of magnitude higher than those in this study. However, large DVC strain uncertainties were reported (MAER above 1500 µε), thus it still remains unclear whether such strain measurements may be largely influenced by noise, as few features (i.e. osteocyte lacunae) may be found within that subvolume size in trabecular bone tissue [86] to allow an accurate DVC computation.

To date, only few studies have been carried out for cortical bone specimens using *in situ* microCT mechanics and DVC [55,87,88], with the present one being the first evaluating cortical tissue mechanics in a continuous fashion. Nevertheless, the measured local average strain of ~−6,000 µε in cortical bone specimens following yielding prior to failure is well aligned to those previously reported from traditional uniaxial compression, which ranged from −6,600 µε to −10,700 µε in the axial direction of human cortical bone [89]. Moreover, the tissue-averaged local strains here presented showed a similar pattern to those measured using high-speed optical imaging and digital image correlation [90], where the strain distribution prior to yielding was approximately constant (i.e. homogeneous distribution) and small but broadened

significantly after it, indicating the onset of high strain regions locally (Figure 8b), that led to failure (Video S7). Peña Fernández et al. [55] recently showed the dynamic strain evolution in cortical bone specimens that had previously been subjected to cyclic loading using the same methodology here reported. Similar to the less cycled specimens therein reported, the specimens used in this study displayed a structural collapse due to the presence of a main longitudinal crack piercing the bone volume longitudinally (Video S7) but higher strains prior to failure, which may be related to some damage already occurring during cyclic loading in [55].

While the overall mechanical behaviour of the synthetics materials was fairly consistent, bone specimens showed a large heterogeneity in their failure modes, which may be explained by their distinct microstructures (i.e., variations in bone volume fraction in trabecular bone specimens) as well as experimental artifacts (i.e., off-axis loading and tilting of cortical bone specimens). Yet, the strain levels prior to failure were in the same range and in line with previous research as discussed above, which confirms the reliability of the proposed experimental approach in examining local mechanics using DVC. Moreover, the ability of DVC to provide local strain measurements in relation to bone microstructure allowed to identify higher compressive strains in trabecular rods compared to trabecular plates prior to failure (Video S6), suggesting the ability of rod-like trabecular structure to sustain higher deformation without causing a catastrophic failure of the structure. Liu et al. [91] conducted a nonlinear micro-finite element (FE) analysis to evaluate the role of trabecular types (i.e. plates and rods) in the failure initiation and progression for human vertebral trabecular bone. It was shown that more trabecular rods failed (i.e., reached tissue strain yielding values) at the initiation of compression while more plates failed around the apparent yielding point, suggesting that local failure initiated primarily at trabecular rods. The high temporal and spatial resolution employed in this study allowed to observe that despite the higher strains, above tissue yielding values, and significant bending prior to fracture in trabecular rods (Figure 11a) failure in the form of fracture occurred at higher strain magnitudes (Figure 7c), whereas plate-like structures failed at lower strain levels (Figure 7d) experiencing some buckling pre-fracture (Figure 11b). These results evidenced the relationships between structure and function in bone tissue, and the importance of local strain measurements to describe and assess the elastic instabilities of bone structure that cannot be entirely described by the material properties of the tissue. However, such relationships were difficult to observe in cortical bone specimens, mainly due to the coarse DVC-resolution (~300 μm), approximately double than the diameter of the osteons in bovine femur [92]. Osteons are complex mechanical features that can act both as stress concentrators, where cracks may initiate (Figure 9a), or as crack propagation barriers (Figure 9b, c). Here, it was observed that some cracks initiated in regions highly strained

(Figure 8c, d), where cortical canals deformed noticeably (Figure 11c), and others developed as a result of an overall structural strain heterogeneity. However, osteon-level strain measurements remain missing and higher-resolution imaging would be needed to provide tissue-level strains [55,87], able to better elucidate the associations between osteons deformation and damage initiation and propagation. Therefore, further improvement of the experimental technique herein presented, mainly imaging and DVC spatial resolution, would be needed to fully characterise the links of bone microstructural features (i.e., trabecular rods and plates, osteons) and local strains leading to the initiation of local failure in bone tissue.
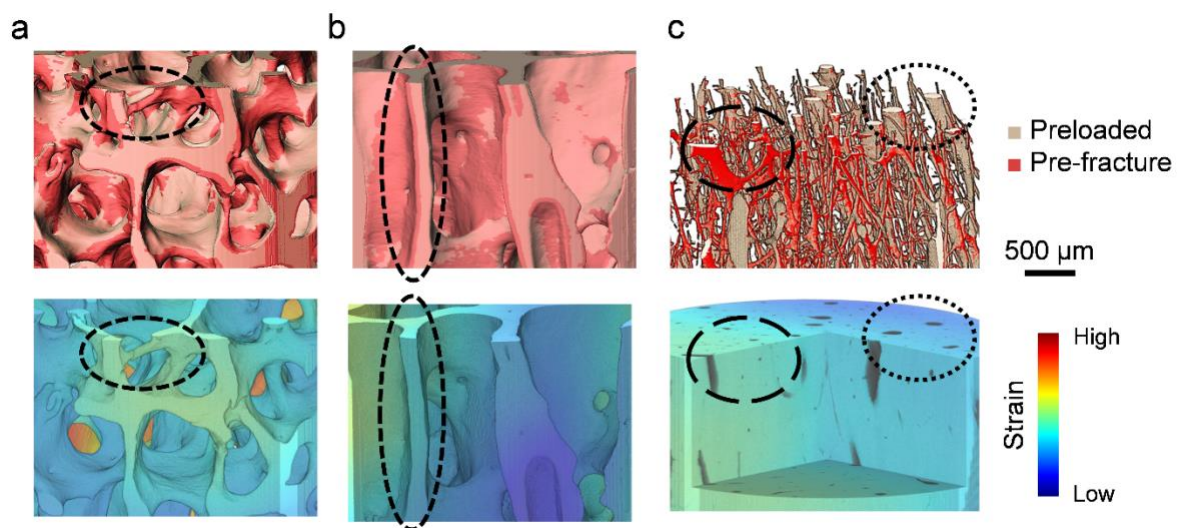

Figure 11. Relationship between microstructure deformation and local strains in (a, b) trabecular and (c) cortical bone specimens. (Top) Differential deformation of pre-fractured (red) SR-microCT images with respect to the preloaded (ivory) ones for trabecular rods in (a) TB#3 specimen, trabecular plates in (b) TB#2 specimen and cortical canals in (c) CB#1 specimens. (Bottom) The strain distribution prior to fracture allowed to identify higher local strain in trabecular rods (a, oval) compared to trabecular bone plates (b, oval). Higher deformation of cortical bone vasculature (c, top, dashed oval) was observed in highly strained regions (c, bottom, dashed oval), while less deformed canals (c, top, dotted oval) experienced lower strains (c, bottom, dotted oval).

Unfortunately, it is known that high exposures to SR X-ray radiation lead to a loss of mechanical and structural integrity of bone as a result of collagen matrix degradation [93,94]; therefore, the radiation dose absorbed by the specimens needs to be considered when performing *in situ* SR-microCT mechanical tests. Here, the experimental session at Diamond Light Source (I13-2) was planned to ensure that specific environmental and technical aspects (e.g., loading stage, filters) were in line to those of previous work from the authors [57,58], from which the radiation doses were estimated, resulting in 34.81 Gy/s and 45.27 Gy/s for cortical and trabecular bone specimens, respectively. Thus, the total radiation dose was below 20.1 kGy during the continuous testing in the present study (Table S2) and far below the currently define 'safe' threshold of 35 kGy [94]); hence, minimising irradiation-induced damage

[58,94]. Nevertheless, it must be noted that the dose estimation considered bone specimens as homogeneous cylinders with a specific apparent density, which may underestimate local dose deposition and consequent damage, particularly in trabecular bone specimens. Specimen-dependent dose simulation may provide further insight on the effect of SR X-ray radiation on the mechanical weakening of bone; however, this was beyond the aims of this study. Further investigations are, therefore, encouraged to better understand the mechanisms leading to collagen degradation and how the X-ray beam-induced thermal gradients [88] contribute to the tissue deterioration. Likewise, the radiation dose absorbed by the cuttlebone specimen could not be estimated due to a lack of data (i.e., energy and flux). Similar to collagen in bone, β-chitin, the main protein in the organic matrix of cuttlebone, is very sensitive to radiation damage [95]. However, the organic matter in cuttlebone is much lower than in bone (~ 4% in cuttlebone, 30% in bone), so the radiation dose needed to deteriorate cuttlebone integrity may be higher than for bone and it is therefore within reason to assume the tissue did not undergo any significant denaturation. This also remains object of future experiments aiming to fully characterise the mechanical behaviour of cuttlebone.

The study of the time-dependent viscoelastic deformation of bone is of great clinical interest to better understand non-traumatic-fractures due to prolonged load over time, loosening of orthopaedic implants due to cyclic loads or the energy absorption and dissipation ability of bone during dynamic loading [96–99]. As such, creep and stress relaxation tests have been previously used to characterise the viscoelasticity of bone [34]. However, it is also known that the mechanical response of bone highly depends on its microarchitecture. Therefore, some studies have developed microFE models of bone accounting for the viscoelasticity of the tissue and validated against creep and stress relaxation experiments [38,100]. However, a validation of local measurements remains missing due to the lack of 3D experimental data. In that perspective, the results herein presented would be highly beneficial to inform, refine and validate such models. Moreover, the combination of continuous *in situ* SR-microCT mechanics and DVC will allow to quantify the local deformation causing both creep and stress relaxation. In this context, Haug et al. [49] recently showed the DVC-computed local displacements and their evolution over time of agglomerates during stress relaxation of vaterite compacts imaged at high temporal (i.e. 18 s) and spatial (0.1625 μm voxel size) resolution using SR light. Such experimental technique and results are therefore encouraging in the field of biomechanics to better understand the time-dependent mechanical behaviour of bone and biomaterials. As such, further optimisation of imaging acquisition and reconstruction algorithms [41] as well as experimental setups minimising irradiation-induced damage [57] are needed to enable the mechanical reproduction of relevant physiological strain rates [101] to fully characterise the long-term effects, larger viscoelastic behaviour and local micromechanics of biomaterials and,

consequently, to extend the technique to softer biological tissues displaying higher viscoelasticity [26,27].

5. Conclusion

Time-resolved *in situ* SR-microCT mechanics and DVC were used to achieve unprecedented qualitative and quantitative analysis of the compressive deformation for bone and bone analogues. The results showed how continuous mechanical testing allowed the dynamic deformation of porous viscoelastic materials to be characterised, enhancing and complementing the information obtained from traditional time-lapsed testing. High-speed SR-microCT imaging was essential to elucidate the relationship between local strains and both damage initiation and propagation during uniaxial compression of biostructures undergoing plastic deformation, bending and/or buckling of their main microstructural elements. The findings of this article highlight the importance of *in situ* SR-microCT dynamic experiments for characterising the time-dependent mechanical behaviour of biomaterials. This has the potential to better inform the effects of clinical conditions on the biomechanical responses of biological tissues.

Conflict of interest statement

F.W. is an employee of Biotrics Bioimplants AG which partially funded this study. The remaining authors declare that they have no known conflict of interests.

Data availability statement

Raw data were generated at Diamond Light Source, I13-2 beamline. Derived data supporting the findings of this study and scripts used to postprocess the data are available on request from the corresponding author, M.P.F.

References

[1]   J.Y. Rho, L. Kuhn-Spearing, P. Zioupos, Mechanical properties and the hierarchical structure of bone, Med. Eng. Phys. 20 (1998) 92–102. https://doi.org/10.1016/S1350-4533(98)00007-1.

[2]   P. Datta, V. Vyas, S. Dhara, A.R. Chowdhury, A. Barui, Anisotropy Properties of Tissues: A Basis for Fabrication of Biomimetic Anisotropic Scaffolds for Tissue Engineering, J. Bionic Eng. 16 (2019) 842–868. https://doi.org/10.1007/s42235-019-0101-9.

[3]   L. Edgar, K. McNamara, T. Wong, R. Tamburrini, R. Katari, G. Orlando, Heterogeneity of Scaffold Biomaterials in Tissue Engineering, Materials (Basel). 9 (2016) 332. https://doi.org/10.3390/ma9050332.

[4]   K. Bobe, E. Willbold, I. Morgenthal, O. Andersen, T. Studnitzky, J. Nellesen, W. Tillmann, C. Vogt, K. Vano, F. Witte, In vitro and in vivo evaluation of biodegradable, open-porous scaffolds made of sintered magnesium W4 short fibres, Acta Biomater. 9 (2013) 8611–8623. https://doi.org/10.1016/j.actbio.2013.03.035.

[5]   S. Gómez, M.D. Vlad, J. López, M. Navarro, E. Fernández, Characterization and three-dimensional reconstruction of synthetic bone model foams, Mater. Sci. Eng. C. 33 (2013) 3329–3335. https://doi.org/10.1016/j.msec.2013.04.013.

[6]   S. Bailey, D. Vashishth, Mechanical Characterization of Bone: State of the Art in Experimental Approaches—What Types of Experiments Do People Do and How Does One Interpret the Results?, Curr. Osteoporos. Rep. 16 (2018) 423–433. https://doi.org/10.1007/s11914-018-0454-8.

[7]   S.R. Goodyear, R.M. Aspden, Mechanical Properties of Bone Ex Vivo, in: R.S. Helfrich M. (Ed.), Bone Res. Protoc. Methods Mol. Biol. (Methods Protoc. Vol 816., Humana Press, Totowa, NJ, 2012: pp. 555–571. https://doi.org/10.1007/978-1-61779-415-5_35.

[8]   C. Jelen, G. Mattei, F. Montemurro, C. De Maria, M. Mattioli-Belmonte, G. Vozzi, Bone scaffolds with homogeneous and discrete gradient mechanical properties, Mater. Sci. Eng. C. 33 (2013) 28–36. https://doi.org/10.1016/j.msec.2012.07.046.

[9]   A. Herrera, J. Hellwig, H. Leemhuis, R. von Klitzing, I. Heschel, G.N. Duda, A. Petersen, From macroscopic mechanics to cell-effective stiffness within highly aligned macroporous collagen scaffolds, Mater. Sci. Eng. C. 103 (2019) 109760. https://doi.org/10.1016/j.msec.2019.109760.

[10]   H. Jin, W.Y. Lu, S. Scheffel, T.D. Hinnerichs, M.K. Neilsen, Full-field characterization of mechanical behavior of polyurethane foams, Int. J. Solids Struct. 44 (2007) 6930–6944. https://doi.org/10.1016/j.ijsolstr.2007.03.018.

[11]   P.S.D. Patel, D.E.T. Shepherd, D.W.L. Hukins, Compressive properties of

commercially available polyurethane foams as mechanical models for osteoporotic human cancellous bone, BMC Musculoskelet. Disord. 9 (2008) 5–11. https://doi.org/10.1186/1471-2474-9-137.

[12]   R. Belda, R. Megías, N. Feito, A. Vercher-Martínez, E. Giner, Some practical considerations for compression failure characterization of open-cell polyurethane foams using digital image correlation, Sensors (Switzerland). 20 (2020) 1–21. https://doi.org/10.3390/s20154141.

[13]   M.L. Bouxsein, Bone quality: where do we go from here?, Osteoporos. Int. 14 (2003) 118–127. https://doi.org/10.1007/s00198-003-1489-x.

[14]   T.M. Keaveny, E.F. Morgan, G.L. Niebur, O.C. Yeh, Biomechanics of trabecular bone, Annu. Rev. Biomed. Eng. 3 (2001) 307–333. https://doi.org/10.1146/annurev.bioeng.3.1.307.

[15]   L. Cristofolini, In vitro evidence of the structural optimization of the human skeletal bones, J. Biomech. 48 (2015) 787–796. https://doi.org/10.1016/j.jbiomech.2014.12.010.

[16]   S.D. Badilatti, P. Christen, I. Parkinson, R. Müller, Load-adaptive bone remodeling simulations reveal osteoporotic microstructural and mechanical changes in whole human vertebrae, J. Biomech. 49 (2016) 3770–3779. https://doi.org/10.1016/j.jbiomech.2016.10.002.

[17]   A. Levchuk, A. Zwahlen, C. Weigt, F.M. Lambers, S.D. Badilatti, F.A. Schulte, G. Kuhn, R. Müller, The Clinical Biomechanics Award 2012 - Presented by the European Society of Biomechanics: Large scale simulations of trabecular bone adaptation to loading and treatment, Clin. Biomech. 29 (2014) 355–362. https://doi.org/10.1016/j.clinbiomech.2013.12.019.

[18]   C.M.J. de Bakker, W.-J. Tseng, Y. Li, H. Zhao, X.S. Liu, Clinical Evaluation of Bone Strength and Fracture Risk, Curr. Osteoporos. Rep. 15 (2017) 32–42. https://doi.org/10.1007/s11914-017-0346-3.

[19]   G. Graziani, M. Berni, A. Gambardella, M. De Carolis, M.C. Maltarello, M. Boi, G. Carnevale, M. Bianchi, Fabrication and characterization of biomimetic hydroxyapatite thin films for bone implants by direct ablation of a biogenic source, Mater. Sci. Eng. C. 99 (2019) 853–862. https://doi.org/10.1016/j.msec.2019.02.033.

[20]   T.L. Mueller, S.E. Basler, R. Müller, G.H. Van Lenthe, Time-lapsed imaging of implant fixation failure in human femoral heads, Med. Eng. Phys. 35 (2013) 636–643.

https://doi.org/10.1016/j.medengphy.2012.07.009.

[21]   M. Peña Fernández, F. Witte, G. Tozzi, Applications of X-ray computed tomography
        for the evaluation of biomaterial-mediated bone regeneration in critical-sized defects,
        J. Microsc. 00 (2019) jmi.12844. https://doi.org/10.1111/jmi.12844.

[22]   C.M. Disney, P.D. Lee, J.A. Hoyland, M.J. Sherratt, B.K. Bay, A review of techniques
        for visualising soft tissue microstructure deformation and quantifying strain Ex Vivo, J.
        Microsc. 00 (2018) 1–15. https://doi.org/10.1111/jmi.12701.

[23]   M. Peña Fernández, A.H. Barber, G.W. Blunn, G. Tozzi, A.A. Fern, Optimization of
        digital volume correlation computation in SR-microCT images of trabecular bone and
        bone-biomaterial systems, J. Microsc. 272 (2018) 213–228.
        https://doi.org/10.1111/jmi.12745.

[24]   E. Dall'Ara, M. Peña-Fernández, M. Palanca, M. Giorgi, L. Cristofolini, G. Tozzi,
        Precision of DVC approaches for strain analysis in bone imaged with μCT at different
        dimensional levels, Front. Mater. 4:31 (2017).
        https://doi.org/10.3389/fmats.2017.00031.

[25]   M. Peña Fernández, C. Black, J. Dawson, D. Gibbs, J. Kanczler, R.O.C. Oreffo, G.
        Tozzi, Exploratory Full-Field Strain Analysis of Regenerated Bone Tissue from
        Osteoinductive Biomaterials, Materials (Basel). 13 (2020) 168.
        https://doi.org/10.3390/ma13010168.

[26]   C.M. Disney, A. Eckersley, J.C. McConnell, H. Geng, A.J. Bodey, J.A. Hoyland, P.D.
        Lee, M.J. Sherratt, B.K. Bay, Synchrotron tomography of intervertebral disc
        deformation quantified by digital volume correlation reveals microstructural influence
        on strain patterns, Acta Biomater. 92 (2019) 290–304.
        https://doi.org/https://doi.org/10.1016/j.actbio.2019.05.021.

[27]   H. Arora, A. Nila, K. Vitharana, J.M. Sherwood, T.T.N. Nguyen, A. Karunaratne, I.K.
        Mohammed, A.J. Bodey, P.J. Hellyer, D.R. Overby, R.C. Schroter, D. Hollis,
        Microstructural consequences of blast lung injury characterized with digital volume
        correlation, Front. Mater. 4 (2017). https://doi.org/10.3389/fmats.2017.00041.

[28]   G. Tozzi, M.P. Fernández, S. Davis, A. Karali, A.P. Kao, G. Blunn, Full-field strain
        uncertainties and residuals at the cartilage-bone interface in unstained tissues using
        propagation-based phase-contrast XCT and digital volume correlation, Materials
        (Basel). 13 (2020) 1–15. https://doi.org/10.3390/ma13112579.

[29]   G. Tozzi, E. Dall, M. Palanca, M. Curto, F. Innocente, L. Cristofolini, Strain

uncertainties from two digital volume correlation approaches in prophylactically augmented vertebrae : Local analysis on bone and cement- bone microstructures, J. Mech. Behav. Biomed. Mater. 67 (2017) 117–126. https://doi.org/10.1016/j.jmbbm.2016.12.006.

[30]   M. Peña Fernández, E. Dall'Ara, A.J. Bodey, R. Parwani, A.H. Barber, G.W. Blunn, G. Tozzi, Full-Field Strain Analysis of Bone–Biomaterial Systems Produced by the Implantation of Osteoregenerative Biomaterials in an Ovine Model, ACS Biomater. Sci. Eng. 5 (2019) 2543–2554. https://doi.org/10.1021/acsbiomaterials.8b01044.

[31]   V. Danesi, G. Tozzi, L. Cristofolini, Application of digital volume correlation to study the efficacy of prophylactic vertebral augmentation, Clin. Biomech. 39 (2016) 14–24. https://doi.org/10.1016/j.clinbiomech.2016.07.010.

[32]   A. Nazarian, R. Müller, Time-lapsed microstructural imaging of bone failure behavior, J. Biomech. 37 (2004) 55–65. https://doi.org/10.1016/S0021-9290(03)00254-9.

[33]   P.J. Thurner, P. Wyss, R. Voide, M. Stauber, M. Stampanoni, U. Sennhauser, R. Müller, Time-lapsed investigation of three-dimensional failure and damage accumulation in trabecular bone using synchrotron light, Bone. 39 (2006) 289–299. https://doi.org/10.1016/j.bone.2006.01.147.

[34]   D. Huang, Y. Huang, Y. Xiao, X. Yang, H. Lin, G. Feng, X. Zhu, X. Zhang, Viscoelasticity in natural tissues and engineered scaffolds for tissue reconstruction, Acta Biomater. 97 (2019) 74–92. https://doi.org/10.1016/j.actbio.2019.08.013.

[35]   D.G. Kim, S.S. Huja, H.R. Lee, B.C. Tee, S. Hueni, Relationships of viscosity with contact hardness and modulus of bone matrix measured by nanoindentation, J. Biomech. Eng. 132 (2010) 1–5. https://doi.org/10.1115/1.4000936.

[36]   M. Unal, A. Creecy, J.S. Nyman, The Role of Matrix Composition in the Mechanical Behavior of Bone, Curr. Osteoporos. Rep. 16 (2018) 205–215. https://doi.org/10.1007/s11914-018-0433-0.

[37]   S. Xie, K. Manda, R.J. Wallace, F. Levrero-Florencio, A.H.R.W. Simpson, P. Pankaj, Time Dependent Behaviour of Trabecular Bone at Multiple Load Levels, Ann. Biomed. Eng. 45 (2017) 1219–1226. https://doi.org/10.1007/s10439-017-1800-1.

[38]   K. Manda, R.J. Wallace, S. Xie, F. Levrero-Florencio, P. Pankaj, Nonlinear viscoelastic characterization of bovine trabecular bone, Environ. Econ. Policy Stud. 16 (2017) 173–189. https://doi.org/10.1007/s10237-016-0809-y.

[39] J.Y. Buffiere, E. Maire, J. Adrien, J.P. Masse, E. Boller, In situ experiments with X ray tomography: An attractive tool for experimental mechanics, Proc. Soc. Exp. Mech. Inc. 67 (2010) 289–305. https://doi.org/10.1007/s11340-010-9333-7.

[40] E. Maire, P.J. Withers, Quantitative X-ray tomography, Int. Mater. Rev. 59 (2014) 1–43. https://doi.org/10.1179/1743280413Y.0000000023.

[41] T. De Schryver, M. Dierick, M. Heyndrickx, J. Van Stappen, M.A. Boone, L. Van Hoorebeke, M.N. Boone, Motion compensated micro-CT reconstruction for in-situ analysis of dynamic processes, Sci. Rep. 8 (2018) 1–10. https://doi.org/10.1038/s41598-018-25916-5.

[42] D. Kytýř, P. Zlámal, P. Koudelka, T. Fíla, N. Krčmářová, I. Kumpová, D. Vavřík, A. Gantar, S. Novak, Deformation analysis of gellan-gum based bone scaffold using on-the-fly tomography, Mater. Des. 134 (2017) 400–417. https://doi.org/10.1016/j.matdes.2017.08.036.

[43] T. Bultreys, M.A. Boone, M.N. Boone, T. De Schryver, B. Masschaele, L. Van Hoorebeke, V. Cnudde, Fast laboratory-based micro-computed tomography for pore-scale research: Illustrative experiments and perspectives on the future, Adv. Water Resour. 95 (2016) 341–351. https://doi.org/10.1016/j.advwatres.2015.05.012.

[44] C. Jailin, S. Roux, Dynamic tomographic reconstruction of deforming volumes, Materials (Basel). 11 (2018). https://doi.org/10.3390/ma11081395.

[45] M. Di Michiel, J.M. Merino, D. Fernandez-Carreiras, T. Buslaps, V. Honkimäki, P. Falus, T. Martins, O. Svensson, Fast microtomography using high energy synchrotron radiation, Rev. Sci. Instrum. 76 (2005). https://doi.org/10.1063/1.1884194.

[46] E. Maire, P.J. Withers, Quantitative X-ray tomography, Int. Mater. Rev. 59 (2014) 1–43. https://doi.org/10.1179/1743280413Y.0000000023.

[47] J. Villanova, R. Daudin, P. Lhuissier, D. Jauffrès, S. Lou, C.L. Martin, S. Labouré, R. Tucoulou, G. Martínez-Criado, L. Salvo, Fast in situ 3D nanoimaging: a new tool for dynamic characterization in materials science, Mater. Today. 20 (2017) 354–359. https://doi.org/10.1016/j.mattod.2017.06.001.

[48] A. Nommeots-Nomm, C. Ligorio, A.J. Bodey, B. Cai, J.R. Jones, P.D. Lee, G. Poologasundarampillai, Four-dimensional imaging and quantification of viscous flow sintering within a 3D printed bioactive glass scaffold using synchrotron X-ray tomography, Mater. Today Adv. 2 (2019) 100011. https://doi.org/10.1016/j.mtadv.2019.100011.

[49]   M. Haug, F. Bouville, J. Adrien, A. Bonnin, E. Maire, A.R. Studart, Multiscale deformation processes during cold sintering of nanovaterite compacts, Acta Mater. 189 (2020) 266–273. https://doi.org/10.1016/j.actamat.2020.02.054.

[50]   Y. Chen, S.J. Clark, C.L.A. Leung, L. Sinclair, S. Marussi, M.P. Olbinado, E. Boller, A. Rack, I. Todd, P.D. Lee, In-situ Synchrotron imaging of keyhole mode multi-layer laser powder bed fusion additive manufacturing, Appl. Mater. Today. 20 (2020) 100650. https://doi.org/10.1016/j.apmt.2020.100650.

[51]   K.M. Kareh, P.D. Lee, R.C. Atwood, T. Connolley, C.M. Gourlay, Revealing the micromechanisms behind semi-solid metal deformation with time-resolved X-ray tomography, Nat. Commun. 5 (2014) 1–7. https://doi.org/10.1038/ncomms5464.

[52]   B. Cai, S. Karagadde, L. Yuan, T.J. Marrow, T. Connolley, P.D. Lee, In situ synchrotron tomographic quantification of granular and intragranular deformation during semi-solid compression of an equiaxed dendritic Al-Cu alloy, Acta Mater. 76 (2014) 371–380. https://doi.org/10.1016/j.actamat.2014.05.035.

[53]   W. Wang, E. Guo, A.B. Phillion, D.G. Eskin, T. Wang, P.D. Lee, Semi-solid compression of nano/micro-particle reinforced Al-Cu composites: An in situ synchrotron tomographic study, Materialia. 12 (2020). https://doi.org/10.1016/j.mtla.2020.100817.

[54]   B. Cai, P.D. Lee, S. Karagadde, T.J. Marrow, T. Connolley, Time-resolved synchrotron tomographic quantification of deformation during indentation of an equiaxed semi-solid granular alloy, Acta Mater. 105 (2016) 338–346. https://doi.org/10.1016/j.actamat.2015.11.028.

[55]   M. Peña Fernández, A.P. Kao, F. Witte, H. Arora, G. Tozzi, Low-cycle full-field residual strains in cortical bone and their influence on tissue fracture evaluated via in situ stepwise and continuous X-ray computed tomography, J. Biomech. 113 (2020) 110105. https://doi.org/10.1016/j.jbiomech.2020.110105.

[56]   T.M. Keaveny, R.E. Borchers, L.J. Gibson, W.C. Hayes, Trabecular bone modulus and strenght can depend on specimen geometry, J. Biomech. 26 (1993) 991–1000.

[57]   M. Peña Fernández, E. Dall'Ara, A. Kao, A. Bodey, A. Karali, G. Blunn, A. Barber, G. Tozzi, Preservation of Bone Tissue Integrity with Temperature Control for In Situ SR-MicroCT Experiments, Materials (Basel). 11 (2018) 2155. https://doi.org/10.3390/ma11112155.

[58]   M. Peña Fernández, S. Cipiccia, E. Dall'Ara, A.J. Bodey, R. Parwani, M. Pani, G.W.

Blunn, A.H. Barber, G. Tozzi, Effect of SR-microCT radiation on the mechanical integrity of trabecular bone using in situ mechanical testing and digital volume correlation, J. Mech. Behav. Biomed. Mater. 88 (2018) 109–119. https://doi.org/10.1016/j.jmbbm.2018.08.012.

[59]   C. Rau, U. Wagner, Z. Pešić, A. De Fanis, Coherent imaging at the Diamond beamline I13, Phys. Status Solidi Appl. Mater. Sci. 208 (2011) 2522–2525. https://doi.org/10.1002/pssa.201184272.

[60]   R.C. Atwood, A.J. Bodey, S.W.T. Price, M. Basham, M. Drakopoulos, A high-throughput system for high-quality tomographic reconstruction of large datasets at Diamond Light Source, Philos. Trans. R. Soc. A Math. Phys. Eng. Sci. 373 (2015). https://doi.org/10.1098/rsta.2014.0398.

[61]   N. Wadeson, M. Basham, Savu: A Python-based, MPI Framework for Simultaneous Processing of Multiple, N-dimensional, Large Tomography Datasets, (2016). http://arxiv.org/abs/1610.08015.

[62]   N.T. Vo, R.C. Atwood, M. Drakopoulos, Superior techniques for eliminating ring artifacts in X-ray micro-tomography, Opt. Express. 26 (2018) 28396. https://doi.org/10.1364/oe.26.028396.

[63]   T. Tanaka, H. Kitamura, SPECTRA: A synchrotron radiation calculation code, J. Synchrotron Radiat. 8 (2001) 1221–1228. https://doi.org/10.1107/S090904950101425X.

[64]   W.C.W. Chang, T.M. Christensen, T.P. Pinilla, T.M. Keaveny, Uniaxial yield strains for bovine trabecular bone are isotropic and asymmetric, J. Orthop. Res. 17 (1999) 582–585. https://doi.org/10.1002/jor.1100170418.

[65]   T.M. Wright, W.C. Hayes, Fracture mechanics parameters for compact bone-Effects of density and specimen thickness, J. Biomech. 10 (1977). https://doi.org/10.1016/0021-9290(77)90019-7.

[66]   J.H. Hubbell, S.. Seltzer, Tables of X-Ray Mass Attenuation Coefficients and Mass Energy-Absorption Coefficients (version 1.4), Natl. Inst. Stand. Technol. Gaithersburg, MD. (2004).

[67]   D. Mattes, D.R. Haynor, H. Vesselle, T.K. Lewellyn, W. Eubank, Nonrigid multimodality image registration, Med. Imaging 2001 Image Process. 4322 (2001) 1609–1620. https://doi.org/10.1117/12.431046.

[68] M. Styner, Parametric estimate of intensity inhomogeneities applied to MRI, IEEE Trans. Med. Imaging. 19 (2000) 153–165. https://doi.org/10.1109/42.845174.

[69] P. Perona, J. Malik, Scale-space and edge detection using anisotropic diffusion, IEEE Trans. Pattern Anal. Mach. Intell. 12 (1990) 629–639. https://doi.org/10.1109/34.56205.

[70] G. Gerig, O. Kbler, R. Kikinis, F.A. Jolesz, Nonlinear Anisotropic Filtering of MRI Data, IEEE Trans. Med. Imaging. 11 (1992) 221–232. https://doi.org/10.1109/42.141646.

[71] S. Berg, D. Kutra, T. Kroeger, C.N. Straehle, B.X. Kausler, C. Haubold, M. Schiegg, J. Ales, T. Beier, M. Rudy, K. Eren, J.I. Cervantes, B. Xu, F. Beuttenmueller, A. Wolny, C. Zhang, U. Koethe, F.A. Hamprecht, A. Kreshuk, Ilastik: Interactive Machine Learning for (Bio)Image Analysis, Nat. Methods. 16 (2019) 1226–1232. https://doi.org/10.1038/s41592-019-0582-9.

[72] M. Doube, M.M. Klosowski, I. Arganda-Carreras, F.P. Cordelières, R.P. Dougherty, J.S. Jackson, B. Schmid, J.R. Hutchinson, S.J. Shefelbine, BoneJ: Free and extensible bone image analysis in ImageJ, Bone. 47 (2010) 1076–1079. https://doi.org/10.1016/j.bone.2010.08.023.

[73] J. Schindelin, I. Arganda-Carreras, E. Frise, V. Kaynig, M. Longair, T. Pietzsch, S. Preibisch, C. Rueden, S. Saalfeld, B. Schmid, J.-Y. Tinevez, D.J. White, V. Hartenstein, K. Eliceiri, P. Tomancak, A. Cardona, Fiji: an open-source platform for biological-image analysis, Nat Meth. 9 (2012) 676–682. https://doi.org/10.1038/nmeth.2019.

[74] M. Peña Fernández, A.H. Barber, G.W. Blunn, G. Tozzi, Optimization of digital volume correlation computation in SR-microCT images of trabecular bone and bone-biomaterial systems, J. Microsc. 272 (2018) 213–228. https://doi.org/10.1111/jmi.12745.

[75] M. Palanca, G. Tozzi, L. Cristofolini, M. Viceconti, E. Dall'Ara, Three-Dimensional Local Measurements of Bone Strain and Displacement: Comparison of Three Digital Volume Correlation Approaches, J. Biomech. Eng. 137 (2015) 1–14. https://doi.org/10.1115/1.4030174.

[76] M. Palanca, L. Cristofolini, E. Dall'Ara, M. Curto, F. Innocente, V. Danesi, G. Tozzi, Digital volume correlation can be used to estimate local strains in natural and augmented vertebrae: an organ-level study, J. Biomech. 49 (2016) 3882–3890. https://doi.org/10.1016/j.jbiomech.2016.10.018.

[77] L. North, D. Labonte, M.L. Oyen, M.P. Coleman, H.B. Caliskan, R.E. Johnston, Interrelated chemical-microstructural-nanomechanical variations in the structural units of the cuttlebone of Sepia officinalis, APL Mater. 5 (2017) 116103. https://doi.org/10.1063/1.4993202.

[78] G. Tozzi, V. Danesi, M. Palanca, L. Cristofolini, Elastic Full-Field Strain Analysis and Microdamage Progression in the Vertebral Body from Digital Volume Correlation, Strain. 52 (2016) 446–455. https://doi.org/10.1111/str.12202.

[79] F. Gillard, R. Boardman, M. Mavrogordato, D. Hollis, I. Sinclair, F. Pierron, M. Browne, The application of digital volume correlation (DVC) to study the microstructural behaviour of trabecular bone during compression, J. Mech. Behav. Biomed. Mater. 29 (2014) 480–499. https://doi.org/10.1016/j.jmbbm.2013.09.014.

[80] B.K. Bay, T.S. Smith, D.P. Fyhrie, M. Saad, Digital volume correlation: Three-dimensional strain mapping using X-ray tomography, Exp. Mech. 39 (1999) 217–226. https://doi.org/10.1007/BF02323555.

[81] M. Peña Fernández, E. Dall'Ara, A.J. Bodey, R. Parwani, A.H. Barber, G.W. Blunn, G. Tozzi, Full-Field Strain Analysis of Bone-Biomaterial Systems Produced by the Implantation of Osteoregenerative Biomaterials in an Ovine Model, ACS Biomater. Sci. Eng. 5 (2019) 2543–2554. https://doi.org/10.1021/acsbiomaterials.8b01044.

[82] E. Dall'Ara, D. Barber, M. Viceconti, About the inevitable compromise between spatial resolution and accuracy of strain measurement for bone tissue: A 3D zero-strain study, J. Biomech. 47 (2014) 2956–2963. https://doi.org/10.1016/j.jbiomech.2014.07.019.

[83] H.H. Bayraktar, E.F. Morgan, G.L. Niebur, G.E. Morris, E.K. Wong, T.M. Keaveny, Comparison of the elastic and yield properties of human femoral trabecular and cortical bone tissue, J. Biomech. 37 (2004) 27–35. https://doi.org/10.1016/S0021-9290(03)00257-4.

[84] G.L. Niebur, M.J. Feldstein, J.C. Yuen, T.J. Chen, T.M. Keaveny, High-resolution finite element models with tissue strength asymmetry accurately predict failure of trabecular bone, J. Biomech. 33 (2000) 1575–1583. https://doi.org/10.1016/S0021-9290(00)00149-4.

[85] M.J. Turunen, S. Le Cann, E. Tudisco, G. Lovric, A. Patera, S.A. Hall, H. Isaksson, Sub-trabecular strain evolution in human trabecular bone, Sci. Rep. 10 (2020) 1–14. https://doi.org/10.1038/s41598-020-69850-x.

[86]   E.N. Cresswell, T.M. Nguyen, M.W. Horsfield, A.J. Alepuz, T.A. Metzger, G.L. Niebur, C.J. Hernandez, Mechanically induced bone formation is not sensitive to local osteocyte density in rat vertebral cancellous bone, J. Orthop. Res. 36 (2018) 672–681. https://doi.org/10.1002/jor.23606.

[87]   D. Christen, A. Levchuk, S. Schori, P. Schneider, S.K. Boyd, R. Müller, Deformable image registration and 3D strain mapping for the quantitative assessment of cortical bone microdamage, J. Mech. Behav. Biomed. Mater. 8 (2012) 184–193. https://doi.org/10.1016/j.jmbbm.2011.12.009.

[88]   M. Peña Fernández, E. Dall'Ara, A.P. Kao, A.J. Bodey, A. Karali, G.W. Blunn, A.H. Barber, G. Tozzi, Preservation of bone tissue integrity with temperature control for in situ SR-microCT experiments, Materials (Basel). (2018). https://doi.org/under review.

[89]   M.J. Mirzaali, J.J. Schwiedrzik, S. Thaiwichai, J.P. Best, J. Michler, P.K. Zysset, U. Wolfram, Mechanical properties of cortical bone and their relationships with age, gender, composition and microindentation properties in the elderly, Bone. 93 (2016) 196–211. https://doi.org/10.1016/j.bone.2015.11.018.

[90]   G. Benecke, M. Kerschnitzki, P. Fratzl, H.S. Gupta, Digital image correlation shows localized deformation bands in inelastic loading of fibrolamellar bone, J. Mater. Res. 24 (2009) 421–429. https://doi.org/10.1557/jmr.2009.0064.

[91]   X.S. Liu, G. Bevill, T.M. Keaveny, P. Sajda, X.E. Guo, Micromechanical analyses of vertebral trabecular bone based on individual trabeculae segmentation of plates and rods, J. Biomech. 42 (2009) 249–256. https://doi.org/10.1016/j.jbiomech.2008.10.035.

[92]   M. Zedda, R. Babosova, Does the osteon morphology depend on the body mass? A scaling study on macroscopic and histomorphometric differences between cow (Bos taurus) and sheep (Ovis aries), Zoomorphology. 140 (2021) 169–181. https://doi.org/10.1007/s00435-021-00516-6.

[93]   H.D. Barth, E.A. Zimmermann, E. Schaible, S.Y. Tang, T. Alliston, R.O. Ritchie, Characterization of the effects of x-ray irradiation on the hierarchical structure and mechanical properties of human cortical bone, Biomaterials. 32 (2011) 8892–8904. https://doi.org/10.1016/j.biomaterials.2011.08.013.

[94]   H.D. Barth, M.E. Launey, A.A. MacDowell, J.W. Ager, R.O. Ritchie, On the effect of X-ray irradiation on the deformation and fracture behavior of human cortical bone, Bone. 46 (2010) 1475–1485. https://doi.org/10.1016/j.bone.2010.02.025.

[95]   O. Paris, From diffraction to imaging: New avenues in studying hierarchical biological

tissues with x-ray microbeams (Review), Biointerphases. 3 (2008) FB16–FB26. https://doi.org/10.1116/1.2955443.

[96]   T.L. Norman, E.S. Ackerman, T.S. Smith, T.A. Gruen, A.J. Yates, J.D. Blaha, V.L. Kish, Cortical Bone Viscoelasticity and Fixation Strength of Press-Fit Femoral Stems: An In-Vitro Model, J. Biomech. Eng. 128 (2005) 13–17. https://doi.org/10.1115/1.2133766.

[97]   M. Taylor, J. Cotton, P. Zioupos, Finite element simulation of the fatigue behaviour of cancellous bone, Meccanica. 37 (2002) 419–429. https://doi.org/10.1023/A:1020848007201.

[98]   A. Phillips, P. Pankaj, F. May, K. Taylor, C. Howie, A. Usmani, Constitutive models for impacted morsellised cortico-cancellous bone, Biomaterials. 27 (2006) 2162–2170. https://doi.org/10.1016/j.biomaterials.2005.10.034.

[99]   P. Pollintine, J. Luo, B. Offa-Jones, P. Dolan, M.A. Adams, Bone creep can cause progressive vertebral deformity, Bone. 45 (2009) 466–472. https://doi.org/10.1016/j.bone.2009.05.015.

[100] C. Sandino, D.D. McErlain, J. Schipilow, S.K. Boyd, The poro-viscoelastic properties of trabecular bone: A micro computed tomography-based finite element study, J. Mech. Behav. Biomed. Mater. 44 (2015) 1–9. https://doi.org/10.1016/j.jmbbm.2014.12.018.

[101] X. Zhai, J. Gao, Y. Nie, Z. Guo, N. Kedir, B. Claus, T. Sun, K. Fezzaa, X. Xiao, W.W. Chen, Real-time visualization of dynamic fractures in porcine bones and the loading-rate effect on their fracture toughness, J. Mech. Phys. Solids. 131 (2019) 358–371. https://doi.org/10.1016/j.jmps.2019.07.010.